# INSTITUTO POLITÉCNICO NACIONAL

CENTRO DE INVESTIGACIÓN EN CIENCIA APLICADA
Y TECNOLOGÍA AVANZADA UNIDAD LEGARIA


# PHOTOACOUSTIC AND MODULATED PHOTOREFLECTANCE IMAGING OF BIASED INTEGRATED CIRCUITS.

**T E S I S**

Que para obtener el grado de

**DOCTORADO EN TECNOLOGÍA AVANZADA**


PRESENTA

**Ernesto Hernández Rosales**

DIRECTORES

Dr. Ernesto Marín Moares
Dr. Antonio Manoel Mansanares

CICATA

Ciudad de México. Julio, 2017

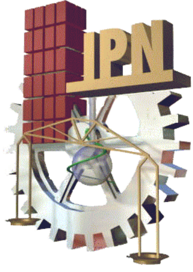


**INSTITUTO POLITÉCNICO NACIONAL**

**Centro de Investigación en Ciencia Aplicada y**

**Tecnología Avanzada Unidad Legaria**

**CICATA-IPN Legaria**

# PHOTOACOUSTIC AND MODULATED PHOTOREFLECTANCE IMAGING OF BIASED INTEGRATED CIRCUITS.

A thesis submitted for the degree of

Doctor of Advanced Technology

PRESENTS

**Ernesto Hernández Rosales**

Thesis advisors

Dr. Ernesto Marín Moares
Dr. Antonio Manoel Mansanares

Ciudad de México. Julio, 2017.

# *INSTITUTO POLITÉCNICO NACIONAL*

## ***SECRETARÍA DE INVESTIGACIÓN Y POSGRADO***

## *CARTA CESIÓN DE DERECHOS*

En la Ciudad de México el día 09 del mes de Junio del año 2017, el que suscribe Ernesto Hernández Rosales alumno del Programa de Doctorado en Tecnología Avanzada con número de registro B130744, adscrito al Centro de Investigación en Ciencia Aplicada y Tecnología Avanzada Unidad Legaria CICATA-Legaria, manifiesta que es autor intelectual del presente trabajo de Tesis bajo la dirección del Dr. Ernesto Marín Moares y el Dr. Antonio Manoel Mansanares y cede los derechos del trabajo intitulado Photoacoustic and modulated photoreflectance imaging of biased integrated circuits, al Instituto Politécnico Nacional para su difusión, con fines académicos y de investigación.

Los usuarios de la información no deben reproducir el contenido textual, gráficas o datos del trabajo sin el permiso expreso del autor y/o director del trabajo. Este puede ser obtenido escribiendo a la siguiente dirección efedora@hotmail.com . Si el permiso se otorga, el usuario deberá dar el agradecimiento correspondiente y citar la fuente del mismo.

M en T.A Ernesto Hernández Rosales

SIP-14-BIS

# INSTITUTO POLITÉCNICO NACIONAL

## SECRETARÍA DE INVESTIGACIÓN Y POSGRADO

*ACTA DE REVISIÓN DE TESIS*

En la Ciudad de México siendo las 12:00 horas del día 09 del mes de Junio del 2017 se reunieron los miembros de la Comisión Revisora de la Tesis, designada por el Colegio de Profesores de Estudios de Posgrado e Investigación de CICATA-Legaria para examinar la tesis titulada:

Photoacoustic and modulated photoreflectance imaging of biased integrated circuits

Presentada por el alumno:

| HERNANDEZ | ROSALES | ERNESTO |
|---|---|---|
| Apellido paterno | Apellido materno | Nombre(s) |

Con registro: | B | 1 | 3 | 0 | 7 | 4 | 4 |

aspirante de:

Doctorado en Tecnología Avanzada

Después de intercambiar opiniones los miembros de la Comisión manifestaron ***APROBAR LA TESIS***, en virtud de que satisface los requisitos señalados por las disposiciones reglamentarias vigentes.

LA COMISIÓN REVISORA

Directores de tesis

Dr. Ernesto Marín Moares

Dr. Antonio Manoel Mansanares

Dr. José Antonio Calderón Arenas

Dr. José Bruno Rojas Trigos

Dr. Salvador Alvarado Ramírez

PRESIDENTE DEL COLEGIO DE PROFESORES

Dra. Mónica Rosalía Jaime Fonseca

CENTRO DE INVESTIGACIÓN EN CIENCIA APLICADA Y TECNOLOGÍA AVANZADA
CICATA - LEGARIA

# ACKNOWLEDGMENTS.

I would like to express my sincere and heartfelt gratitude to all those who directly or indirectly helped in the realization of this work.

I am grateful to my alma mater, the Instituto Politecnico Nacional, for opening its doors during my studies; from high school through my graduate and post-graduate studies.

Especially and firstly I mention my thesis advisor, Dr. Ernesto Marin Moares, for his words of encouragement, for believing me, and for all the wise advices from the beginning of master's degree to the end of my doctorate.

I want to thank my co-director for this doctoral work, Dr. Antonio Manoel Mansanares of UNICAMP, Campinas, SP, Brazil, for making his help available at all times and providing the means for my research stay at the Institute of Physics Gleb Wataghin (IFGW-Unicamp). I am grateful and acknowledge for all the time invested in directing and correcting this thesis, for his excellent advice, and sharing his invaluable knowledge and providing unconditional dedication, and specially for his support in the realization of this thesis. I also thank Dinah for her help provided at Campinas.

I would like to show my appretiation to the whole academic team of CICATA-Legaria: Dr. Fernando Trejo Zárraga, Dra. Rocío Alejandra Muñoz Hernández, Dr. Miguel Ángel Aguilar Frutis, Dra. María de los Ángeles Mantilla among other professors for their time and contribution to my training.

To the people of the photothermics group, to Dr. José Antonio Calderón Arenas, Dr. José Bruno Rojas Trigos, Dr. Gustavo Juarez Gracia and Dr. Salvador Alvarado Ramirez, for the time devoted to this work and their participations as synodal in the degree examination.

My gratitued also goes to all the staff that makes up the Postgraduate Program in Advanced Technology, C. Laura Vega Haro, C. Leticia Cardona Gómez, Ing. Pablo Méndez, for their kind assistance and attention in the course of this doctoral program and to each one of my friends co-generation, for their friendship and collaboration in the laboratory of applied physics. Also I want to express my gratitud to CONACYT, SIP research projects, and the PIFI-IPN program, for the financial support provided during this doctoral program.

And last but not least, I want to thank my girlfriend Paty, my brothers, and other relatives for their support, joy and gave me the strength to go on.

**CONTENT.**


| | | | Page |
|---|---|---|---|
| **Resumen.** | | | iv |
| **Abstract.** | | | v |
| | | Introduction. | 01 |
| | | Hypothesis. | 02 |
| | | General Objective. | 02 |
| | | Particular Objectives. | 03 |
| **CHAPTER 1** | | Photothermal techniques. | 04 |
| | 1.1 | Thermal Waves. | 06 |
| | 1.2 | Fundamental properties of thermal waves. | 08 |
| | 1.3 | Applications of thermal waves. | 10 |
| | 1.4 | Phase Resolved detection method. | 12 |
| **CHAPTER 2** | | Experimental Arrangement. | 14 |
| | 2.1 | Methodology. | 14 |
| | 2.2 | Photoacoustic Microscopy (PAM) with piezoelectric detection. (Thermoacoustic). | 14 |
| | 2.3 | Photoreflectance Microscopy (PRM). | 17 |
| | 2.3.1 | Modulated Photoreflectance. (Laser beam as excitation & Probe laser beam). | 17 |
| | 2.3.2 | The sample as a source of excitation. Joule Heating. (Thermoreflectance). | 20 |
| | 2.4 | Combined Thermoacoustic and Thermoreflectance setup. | 22 |
| **CHAPTER 3** | | Scanning Photoacoustic Microscopy of a Smart Card Chip. | 24 |
| | 3.1 | Imaging of a Smart Card Chip (SCC). | 24 |
| | 3.2 | General considerations of the SCC. | 24 |
| | 3.3 | Results and Discussion. | 27 |

| | | | |
|---|---|---|---|
| **CHAPTER 4** | | Combined PRM and PAM set-up, for imaging unbiased in solar cells and non-encapsulated microelectronics chips. | 31 |
| | 4.1 | General considerations of Solar Cell Assembly SCA. | 31 |
| | 4.1.1 | Results and discussion of the SCA. | 33 |
| | 4.2 | Thick film technology (TFT). Imaging on chip unencapsulated. | 37 |
| | 4.2.1 | General considerations of the TFT on chip. | 37 |
| | 4.2.2 | Results and discussion. | 38 |
| **CHAPTER 5** | | Imaging of Biased Encapsulated Microelectronic circuits using a combined Thermoreflectance and Thermoacoustic set-up. | 40 |
| | 5.1 | Introduction. | 40 |
| | 5.2 | Description of the test chip LACAM-02. | 40 |
| | 5.3 | Imaging on Polysilicon Tracks. | 43 |
| | 5.3.1 | Experimental details. | 44 |
| | 5.3.2 | Results and Discussion. | 44 |
| **Conclusions** | | | 56 |
| **References** | | | 57 |
| Appendix A | | List of Figures. | 61 |
| Appendix B | | List of Tables. | 61 |

# Resumen.

Las fallas en los dispositivos micro y optoelectrónicos son causadas por diferentes causas, una de las más importantes es el aumento de la temperatura debido al calentamiento Joule. La microscopía de reflectancia fototérmica se ha convertido en una técnica bien establecida no sólo para la caracterización de propiedades térmicas (difusividad térmica, conductividad térmica, resistencia térmica interfacial) de materiales de escala micrométrica y para detectar defectos en los materiales utilizándolo como una prueba no destructiva, además de ser utilizado en investigación sobre la distribución del calor en dispositivos opto y microelectrónicos en funcionamiento. Por otra parte, la técnica fotoacústica ha sido utilizada para la obtención de imágenes de circuitos electrónicos sin polarización, para la caracterización de mecanismos de recombinación de portadores y para la medición de la eficiencia de dispositivos.

El objetivo de este trabajo de doctorado es explorar las posibilidades de una técnica alternativa que utilice la técnica de fotoreflectancia en combinación con la técnica fotoacústica para la formación de imágenes en circuitos microelectrónicos polarizados, o no polarizados en celdas solares y otros dispositivos o estructuras electrónicas. Esto implica el desarrollo de instrumentación científica, el modelaje matemático, simulaciones numéricas y validación experimental

# Abstract.

Failures in micro and optoelectronic devices occur because there are different causes, being one of the most important the increase of temperature due to Joule heating. Photothermal reflectance microscopy has become a very well established technique not only for the characterization of thermal properties (thermal diffusivity, thermal conductivity, interfacial thermal resistance) of materials at the micrometer scale and for detecting imaging defects in non-destructive testing, but also for the investigation of the heat source distribution in optoelectronic and microelectronic devices in operation. On the other hand, the photoacoustic technique has been also explored before for imaging non-biased electronic circuits, and its usefulness for characterization of minority carriers recombination mechanisms and device efficiency is well documented.

The aim of this PhD work is to explore the possibilities of an alternative technique that uses a combined photoreflectance and photoacoustic set-up for imaging biased and unbiased microelectronic circuits, solar cells and other devices. This involves the development of scientific instrumentation, mathematical models, numerical simulations, and experimental validation.

# Introduction.

During the last 30-40 years, the physics of thermal waves has been developed and many related photothermal techniques have been implemented very successfully for materials characterization. Different applications have been reported in the fields of thermal characterization, spectroscopy and imaging, among others. This work will be focused in applications related to the imaging of microelectronic circuits.

There are several photothermal techniques used for imaging of microelectronic devices in order to detect hotspots, broken points, delamination's, defects, etc. Most of the authors use the Photothermal reflectance microscopy [1-18] in frequency domain, because it has several advantages over other photothermal imaging techniques.

Among them we can mention:

1- Relative simple and inexpensive experimental set-up and easy instrumentation.
2- It is an all-optical method being, therefore, a non-destructive and non-contact technique.
3- Modulation frequencies are typically in the range of kHz to MHz to bring the characteristic thermal diffusion length to the micrometer and submicrometer scale.
4- The pump and probe lasers (wave-length) can be changed in order to study different physical systems and/or phenomena.
5- Targeting both lasers to a single point or in delay allow different kinds of applications (not only imaging but also measurement of thermal properties and minority electrical carriers transport parameters, study of non-radiative recombination mechanisms in semiconductors, etc.)

On the other hand, among the limitations of the technique we can mention the long data acquisition time and the technical limit imposed to the highest modulation frequencies available (this last limitation is avoided by working in time domain with pulsed lasers of very short time duration, e.g. femtosecond's lasers).

Another photothermal method that have been used for imaging is the photoacoustic technique with piezoelectric detection. This technique has demonstrated its high reliability and ability to perform measurements in different materials [19-21], demonstrating that being the detector in contact with the sample is not a limitation.

In the conventional photoreflectance technique, the lateral resolution (imaging) is naturally achieved by scanning the probe beam on the sample surface. The piezoelectric sensor, on the other hand, detects the heat generated in the sample, both directly (pyroelectric effect) and through acoustic waves coupled to the temperature field (piezoelectric effect), disregarding the location of the heat source. However, it is possible to restore lateral resolution by focusing a non-modulated laser beam on the sample surface. The laser absorption creates an additional modulated signal on the detector that is sensitive to the geometry of the sample structure (namely, distinct material layers linked to the presence of electric current/field/potential).

# Hypothesis.

The photoacoustic method with piezoelectric detection can aids the modulated photoreflectance technique for imaging biased and non-biased microelectronic circuits, because the phenomenon of thermal wave detection is different in each approach and different contributions to the photothermal signal exist.

# General objective.

Design and construction of a combined modulated photoreflectance and photoacoustic microscope for imaging of polarized and non-polarized microelectronic devices.

# Particular objectives.

1. Implementation of a combined modulated photoreflectance and photoacoustic microscopy experimental set-up.
2. Application of the combined microscope for imaging of passive microelectronic devices.
3. Application of the combined microscope for imaging of biased microelectronic devices with thermal wave excitation done by modulated current/voltage applied to the circuits.
4. To demonstrate that a combined modulated photoreflectance and photoacoustic microscopy experimental set-up can be used for imaging.

CHAPTER 1

# Photothermal Techniques.

Photothermal techniques are related to electromagnetic into thermal energy conversion. They are based in a principle of heating the sample under investigation using light and measuring the induced temperature changes. The heating can be continuous or pulsed (a single pulse or a train of pulses, mainly harmonic, at a 50% duty cycle). Part of the energy of the electromagnetic radiation that impinges the sample can be absorbed, and part of the absorbed energy can be transformed into heat. This heat dissipates throughout the sample and the surrounding medium creating a spatial temperature distribution that changes with time following the light intensity modulation. These temperature oscillations are often called thermal waves. They depend on the properties involved in the mechanisms of optical absorption, light into heat energy conversion and heat transfer. The first one depends on properties such as the optical absorption coefficient, which depends on the light wavelength. Therefore, measuring the temperature changes as a function of the photons wavelength allows doing a special kind of optical absorption spectroscopy. The second process depends on the so-called quantum efficiency of the energy conversion process, which is defined as the ratio between generated heat and absorbed electromagnetic energy. This, and other parameters related to the energy conversion process that are particular for each material can be determined in a photothermal experiment. Lastly, the heat transfer processes are determined by thermal properties such as thermal conductivity, diffusivity, effusivity and specific heat. Consequently, a photothermal experiment can be designed to measure these materials properties. The temperature field can be measured directly at a given point of the sample using appropriate sensors, or indirectly, by measuring the changes provoked by heating in temperature dependent properties of the sample itself or of the medium surrounding it.

Each photothermal method gets name according to the particular form used for detection [22]. Two methods are used in this work: The photoacoustic microscopy (PAM) with piezoelectric detection and the Photothermal Reflectance Microscopy (PRM).

In photoacoustics, the periodical thermal expansion that it can proceed thermal waves generation, can produce a pressure wave that will propagate through the medium. Thermal waves are highly damped waves, with micrometer or sub-micrometer wavelength at kHz modulation frequencies. Thus, they can interact with locale regions of the sample of the same size to generate a photothermal signal. The generated information can be carried by millimeter long wavelength non-attenuated acoustic waves to a piezoelectric transducer that detects them. This method exploits the strong optical and thermal contrast within regions with dimensions of about one thermal wavelength, as well as the modulation frequency dependent thermal wave damping, for recording images in a sample´s raster scan mode, unable to be seen by other techniques. This non-invasive imaging technique can be used to visualize both superficial and sub-superficial structures of samples.

In the PRM the sample excitation is provided by an intensity modulated laser beam, which heats the sample through light absorption [23, 24]. The surface temperature of the sample is probed by a second non-modulated laser, whose intensity changes induced by variations in sample optical reflectance provoked by the periodical heating are detected by a photodiode coupled to a lock-in amplifier. Experiments are run by scanning both lasers across the sample surface (imaging).

In both techniques the lasers are focused on the sample surface by an optical microscope to the diffraction limit, reaching diameters of the order of one micrometer. This, ultimately, defines the lateral resolution of the technique. Modulation frequencies are typically in the range of kHz to MHz to bring the characteristic thermal diffusion length to the micrometer scale [13, 17].

It is worth to mention that although the absorption of periodical intensity modulated electromagnetic radiation by the sample is the most useful form used for heating, other variants can be used as well for the same purpose. For example, in part of this work the Joule´s effect has been also used, i.e. for operating devices the excitation was done by modulated current/voltage applied to the circuit.

## 1.1 Thermal Waves.

***Generation and propagation of thermal waves.***

Consider a homogeneous isotropic semi-infinite medium with a superficial uniform periodical heat source of the form $(Q_0/2)[1+cos(\omega t)]$, where $Q_0$ is the source intensity (W/m$^2$), $\omega$ is the angular modulation frequency of the heat source and $t$ is the time [22] (see Fig. 1.1).

If the heating surface is taken to fill the plane $x = 0$, the temperature distribution within the solid $T$ can be obtained by solving a one-dimensional equation for the diffusion equation in $x$ and $t$ :

$$\frac{\partial T^2}{\partial x^2}-\frac{1}{\alpha}\frac{\partial T}{\partial t}=0, \qquad x<0, \quad t>0 \tag{1.1}$$

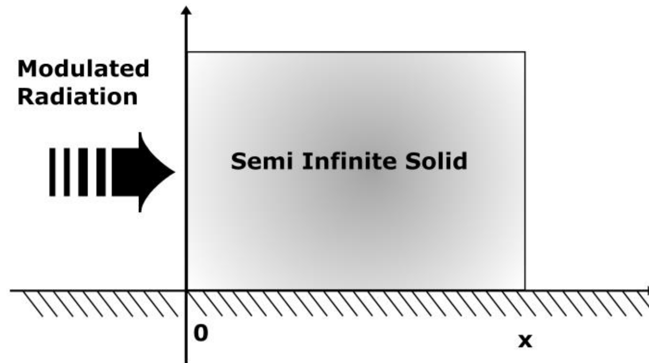


**Fig. 1.1:** A homogeneous solid Semi-infinite uniformly illuminated with a modulated radiation flux at the surface x = 0.

subject to the boundary condition that the energy applied to the surface is dissipated by conduction in the solid, i.e.:

$$-k\left.\frac{\partial T}{\partial x}\right|_{x=0}=\mathrm{Re}\frac{Q_0}{2}\left(\left[1+e^{j\omega t}\right]\right),\quad t>0 \tag{1.2}$$

In the above equations α is the thermal diffusivity, $k$ is the thermal conductivity and $j=\sqrt{-1}$. Note that the heat flow is divided into two parts: $Q_0/2$ y $(Q_0/2)e^{j\omega t}$, where the first represents the stationary component or *dc*, of the flux, while the second refers to the time dependent component or *ac* component. The *dc* component produces a temperature increase and is responsible for transporting energy, while the *ac* component is responsible for harmonic temperature variations. We are interested only in the *ac* component so that the *dc* components will be omitted in what follows. To solve the equation (1.1) we assume that the periodic component has a solution of the form:

$$T(x,t)=\mathrm{Re}\left(\Phi(x)e^{j\omega t}\right) \tag{1.3}$$

substituting (1.3) into equation (1.1), we obtain for all time $t$:

$$\frac{d^2\Phi(x)}{dx^2}-\frac{j\omega}{\alpha}\Phi(x)=0 \tag{1.4}$$

in this way, the spatial dependence of the ac temperature can be written as follows:

$$\Phi(x)=Ae^{(-x\sigma)}+Be^{(x\sigma)},\qquad \sigma=(1+j)\sqrt{\frac{\omega}{2\alpha}} \tag{1.5}$$

where $A$ and $B$ are arbitrary constants and $\sigma$ is called the complex thermal diffusion coefficient. To evaluate these constants, note that when $x$ tends to $+\infty$, $\Phi(x)$ must be finite and therefore the constant $B$ is zero. Applying the boundary condition (1.2), we have:

$$\frac{Q_0}{2}=-k\left.\frac{d\Phi(x)}{dx}\right|_{x=0}=(-k)(-\sigma)A \tag{1.6}$$

and therefore: $= Q_0/2k\sigma$ . Finally obtain the temperature component $T^{ac}$, is given as follows [25]:

$$T^{ac}(x,t) = \frac{Q_0}{2k}\text{Re}\left(\frac{e^{(\omega t-\sigma x)}}{\sigma}\right) = \frac{Q_0}{2\sqrt{\rho c k\omega}}e^{-x\sqrt{\frac{\omega}{2\alpha}}}\cos\left(\omega t - x\sqrt{\frac{\omega}{2\alpha}} - \frac{\pi}{4}\right) = A\cos(\omega t + \Delta\varphi) \quad (1.7)$$

where $c$ is the density, $\rho$ is the specific heat, $C = \rho c$ is the specific heat capacity, $k$ is the thermal conductivity, A is the amplitude and $\Delta\varphi$ is the phase, which are given by

$$A = \frac{Q_0}{2\sqrt{\rho c k\omega}}e^{-x\sqrt{\frac{\omega}{2\alpha}}} \quad \text{and} \quad \Delta\varphi = -x\sqrt{\frac{\omega}{2\alpha}} - \frac{\pi}{4} \quad (1.8)$$

respectively.

## 1.2 Fundamental properties of thermal waves.

The principal characteristics of equation (1.7) are:

**I**. The amplitude of the wave is strongly damped at a distance called the *thermal diffusion length,* $\mu$, which is given by:

$$\mu = \sqrt{\frac{\alpha}{\pi f}} \quad (1.9)$$

At that distance, the thermal wave amplitude decays to a value of $1/e$ of its initial value at $x = 0$. In arriving to Eq. (1.8) convective and radiative heat losses from the sample to its environment have been neglected (they are only important for very low modulation frequencies, [26] being unimportant for those used in this work).

**II**. The wave length and the phase velocity of the thermal wave are, respectively:

$$\lambda = 2\pi\mu \;;\; v = 2\sqrt{\pi\alpha f} \quad (1.10)$$

**III**. There is a phase delay between the periodic warming process and the thermal response given by:

$$\Delta\varphi = -\sqrt{\frac{\pi f}{\alpha}}x - \frac{\pi}{4} \tag{1.11}$$

**IV**. Since the thermal diffusion length $\mu_S$ and the phase delay vary with the modulation frequency, *f,* appropriate frequency modulation can be used for depth profiling. However, the drastic decrease in amplitude caused by the exponential damping factor, has a natural limitation for large penetration depths.

**V**. For a thermal wave propagating from medium 1 to 2, reflection and transmission coefficients at the interface can be defined as:

$$R_{12} = \frac{A_r}{A_i} = \frac{b_{12} - 1}{b_{12} + 1} \tag{1.12}$$

and

$$T_{12} = \frac{A_t}{A_i} = \frac{2b_{12}}{1 + b_{12}} \tag{1.13}$$

respectively, where

$$b_{12} = \frac{\varepsilon_1}{\varepsilon_2} \tag{1.14}$$

is the ratio of the media thermal effusivities.

**VI**. There are two basic thermal parameters governing the behavior of thermal waves. Among thermal diffusivity, $\alpha$, which is the most important parameter for time dependent diffusion processes within homogeneous isotropic materials, the quantity

$$\varepsilon = \sqrt{k\rho c} \tag{1.15}$$

(1.15) is defined as the thermal effusivity or thermal inertia, giving us a measure of the ability of the medium to exchange heat with their environment. This parameter is extremely relevant to the processes of heating and cooling at surfaces and interfaces [27, 28].

## 1.3 Applications of thermal waves.

There are many applications of thermal waves [29]. They are mainly based in the mechanisms involved in the photothermal signal generation mentioned above. Therefore, thermal waves have been widely used for thermal characterization of solids (thermal diffusivity [30, 31], thermal conductivity [32-34]), liquids [35-39], and gaseous [40, 41] samples, for spectroscopy [42, 43], for electronic transport parameters determination and analysis of carrier recombination mechanisms in semiconductors [44-47], among others. Imaging is another interesting field of application [48-52], and we will focus our attention here to this last application.

When periodical modulated electromagnetic radiation interacts with matter a fraction of the energy is absorbed and converted into heat and this in turn leads to the generation of thermal waves [22, 53] among other effects, the subsequent periodical thermal expansion can produce a pressure wave that will propagate through the medium. Thermal waves are highly damped waves, with micrometer or sub-micrometer wavelength at typical modulation frequencies. Thus, they can interact with locale regions of the imaged object of the same size to generate a photothermal signal. The generated information can be detected as changes in the optical reflection of the sample in the photothermal reflectance technique or can be carried out by millimeter long wavelength non-attenuated acoustic waves to a piezoelectric transducer that detects them in the photoacoustic approach. These methods exploit the strong optical and thermal contrast within regions with dimensions of about one thermal wavelength, as well as the modulation frequency dependent thermal wave damping, for recording images in a sample´s raster scan mode and in a non-destructive way, unable to be seen by other techniques.

In the photoacoustic detection the sample is in contact with a piezoelectric detector, which senses the photo-induced thermal expansion of a sample. The transducer converts the strain generated by the thermal waves on its surface to an electrical voltage. Any piezoelectric material manifests also pyroelectricity. A pyroelectric material is one that has the ability to detect changes in temperature. These sensors produce surface electric charges when heated. The electrical signal obtained from them, comes from the removal of this charge by metal electrodes placed on the material surface. Thus, a temperature change in the material produces a change in the polarization charge. An electric signal is proportional to the rate of the charge is then generated. [54, 55]. These sensors can be made from crystals or piezoelectric ceramics such as PZT (Lead Zirconate Titanate), but usually a polymer film of polivinidinil difluoride (PVDF) can be used.

On the other hand, in the modulated photoreflectance approach, the sample optical reflectivity is modulated by the generated thermal waves. The change in reflectance with the temperature is given by

$$\frac{\Delta R}{R_0} = \frac{1}{R_0}\frac{dR}{dT}\Delta T \tag{1.16}$$

where $R_0$ is the sample thermal reflectance at ambient temperature and $\frac{1}{R_0}\frac{dR}{dT}$ is the coefficient of thermal reflectance, which ranges between $10^{-4}$ to $10^{-6}$ per degree for solids [22].

## 1.4 Phase-Resolved detection method.

The basic idea may be summarized as follows. Let us consider a typical photoacoustic spectroscopy (PAS) arrangement in which heat is generated within the sample due to the absorption of chopped radiation. For the sake of the argument, we further assume that the sample is made of two layers of materials $A$ and $B$ with material $A$ facing the gas phase of the PA cell. At a fixed modulation frequency, the acoustic signal detected at the microphone is the resultant of the contributions of the heat generated in both constituents A and B. As the component $B$ is beneath $A$ there should exist a time lag between the signals arising from $A$ and $B$ due to the difference in the corresponding thermal diffusion times. This difference in the time lengths to reach the gas phase produces a phase shift e between the two signals. Thus, the actually observed signal $S$ may be viewed as the resultant of two vectors (whose lengths $S_A$ and $S_B$ correspond to the signals of $A$ and $B$, respectively) with an angle $\theta$ between them. This means that once the angle $\theta$ is known, by varying the phase of 90°, say with respect to the signal $S_A$ one should observe only the contribution of component $B$, and vice versa. In other words, by measuring the phase variation of the photoacoustic (PA) signal of a composite sample one may, in principle, single out the contribution of the different constituents at different locations [56].

Usually, the depth profiling analysis in conventional PAM [57] is carried out by measuring the PA signal at different modulation frequencies. Subsurface locations are then differentiated by the change of the penetration depth of the heat wave with the modulation frequency. The phase-resolved technique, in contrast, measures the PA signal at a constant modulation frequency at various phase angles, i.e., the different subsurface layers are identified by transit time of the heat generated at these locations. The phase-resolved plots are obtained by recording the in-phase component of the PA signal several times, changing the phase angle offset.

It can be demonstrated that for a given phase angle $\psi$ the generated signal, $S$ can be written in terms of the In-phase, $S_0$, and quadrature, $S_{90}$, components as (1.17), (see Fig 1.2).

$$S = S_0 \cos\psi + S_{90} \sin\psi \tag{1.17}$$

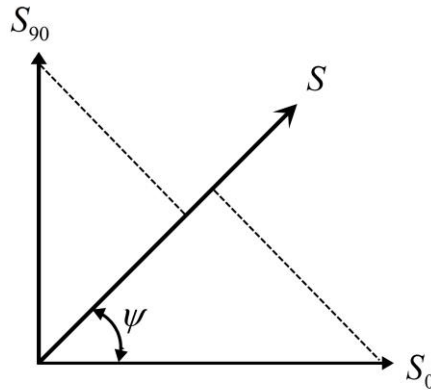


**Fig. 1.2:** PA signal at a phase $\psi$ expressed as the sum of the signal at $0^{\circ}$ and $90^{\circ}$ phases.

CHAPTER

2

# Experimental Arrangement.

## 2.1 Methodology.

Two experimental set-ups have been designed and constructed. A photoacoustic microscope was implemented in the Photothermal Techniques Laboratory at CICATA-Legaria, IPN, Mexico City, Mexico, and an acoustic detection stage was coupled to a photothermal modulated reflectance microscope existing at the Physics Institute of the Campinas State University, UNICAMP, Campinas, SP, Brazil. In both cases, facilities for electrical periodical heating of circuits have been added. Both experimental set-ups were fully automatized for data acquisition.

## 2.2 Photoacoustic Microscopy (PAM), with piezoelectric detection. (Thermoacoustic).

A schematic view of the experimental set-up is shown in Fig. 2.1(a), while in 2.1(b) a photograph is presented. A longstanding optical microscope (ROI - RAM Optical Instruments. Spirit Optical Measurement Inspection Station Model 01-1001-01 mfd. 1996). Was used to implement the device in it. The excitation light source is an IR (785nm) diode laser BWF1 (Edmond-Optics), modulated by a TTL signal (provided by a Lock-in amplifier) to which an optical fiber is coupled. The fiber in turn focuses the light on to the sample. The laser spot has been estimated 105 μm (Multimode) wide. The sample is glued to the piezoelectric transducer using thermal paste assuring a good acoustic and mechanical contact.

The sensor used in this work was the active piezoelectric element of the electronic buzzer model BGD (available at low cost in Mexican Electronic Products Store STEREN) shown in Fig. 2.1(c). It has been found by Energy Dispersive Spectroscopy (EDS) measurements (performed with an Oxford Pentafet X-ray detector coupled to a JEOL JSM-6390LV Scanning Electron Microscope) that it consists on a Lead-Zircon Titanate (PZT) ceramic material (0.481 mm thick) deposited on a copper metal plate (0.323 mm) and with the other surface (in contact with the sample in our experiments) covered with a thin layer of silver. Both metals serve as electrical contact electrodes. It must be noticed that other kinds of piezo-transducers can be used as well. However, due to its robustness, the PZT is easier to handle, to clean, and the loading and unloading of samples becomes simpler. An added bonus is that it is relatively inexpensive. The sample-detector system is mounted onto the X-Y positioning platform of the microscope allowing scanning in both x and y directions with a minimal step of 1 μm using a step motors driver system. In this way, and maintaining fixed the laser position, a previously selected region of the sample can be scanned. The selection of the region of interest is performed in-situ using a camera and video imaging system provided by the optical microscope, which has been coupled to a computer video card and a joystick.

To avoid unwanted heating of the sample, the impinging light power is limited to some mW, so that the temperature oscillations amplitudes are expected to remain well below the absolute sample temperature. They are often limited to a few mK. Consequently, the electrical signals generated by the sensing element are usually very small. They are also generally polluted by noise, making this an ideal scenario for its measurement using synchronous phase sensitive detection with a Lock-in amplifier (LIA). A commercial LIA (SR 830 from Stanford Research Systems) was used. Due to the nature of the sensing element, impedance coupling between it and a LIA must be taken into account. In our set-up a high impedance pre-amplifier stage (Voltage- Amplifier FEMTO DLP) has been used to avoid any problems. The system has been automated using LABView. The laser modulation frequency is fixed at the desired value using the RS-232 port of the LIA and data recording from the LIA takes place using a GPIB (NI-USB/HD) shown in figure 2.1 (a) and (b).

The recorded data (values of the in-Phase and Quadrature or Amplitude and Phase signals as a function of x and y coordinates) can be stored in such a manner that they can be also exported to be handled with programs such as Matlab and Origin.

The system can be also monitored and controlled remotely trough any device with internet access so that physical presence of the operator during the whole data acquisition time is not necessary. Thus, it is possible within one laboratory session to program the measurement, whose results can be collected later and/or remotely in electronic way for data analysis and processing. More details have been given elsewhere [58].

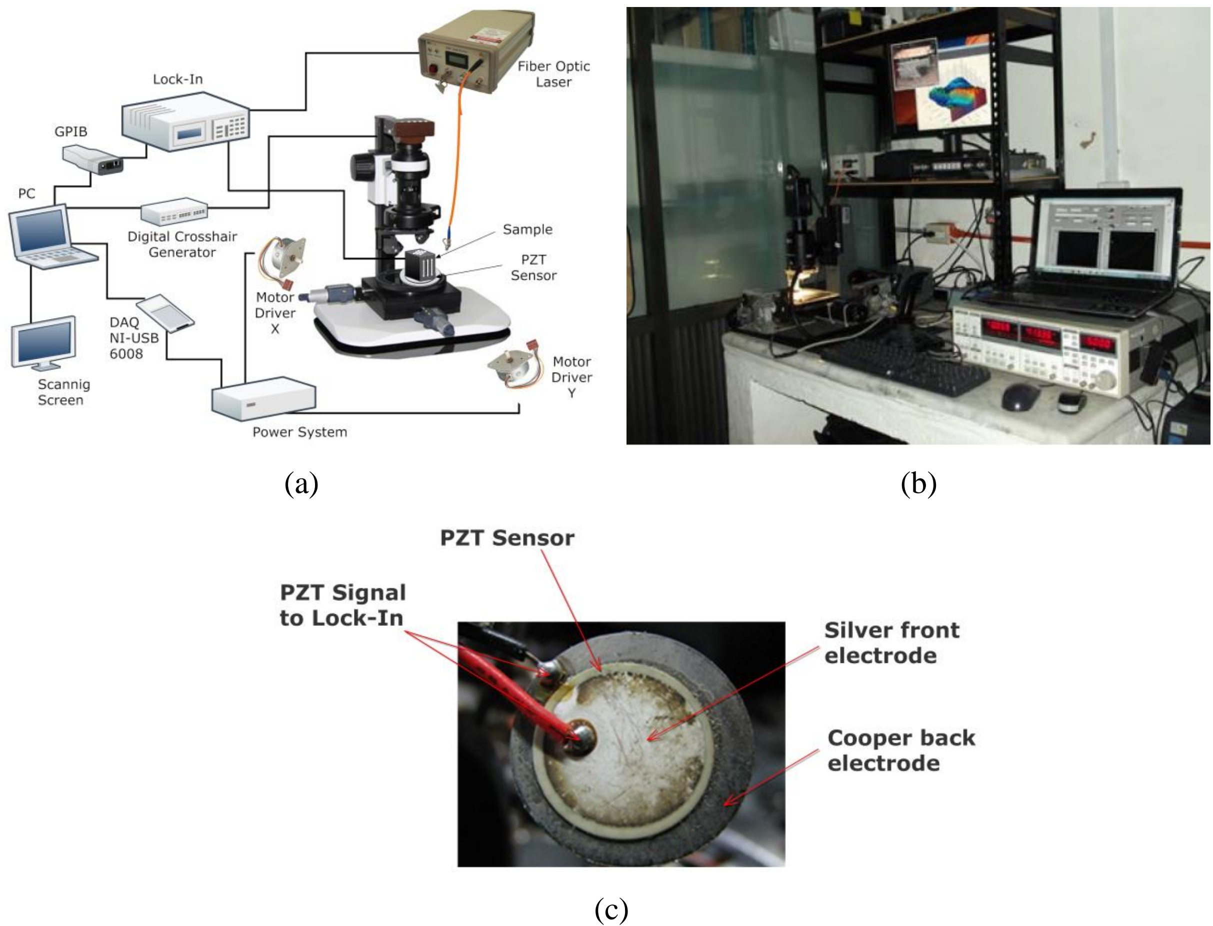


**Fig. 2.1**: Experimental arrangement of Photoacoustic Microscopy, with piezoelectric detection. a) Schema of the photoacoustic microscope b) Photograph of the microscope c) Photograph of the PZT transducer.

## 2.3 Photoreflectance Microscopy (PRM).

### *2.3.1 Modulated Photoreflectance. (Laser beam as excitation & Probe laser beam).*

The Fig. 2.2 shows schematically the experimental setup of the photothermal reflectance technique. The heating device used in the experimental apparatus was an $Ar^+$ ion laser (Stabilite 2017, Spectra-Physics), with nominal power of 7 W.

This laser has spectral lines at the wavelengths , $\lambda_b$, 457.8, 476, 488, 496, 502 and 514.5 nm, being the 488 and 514.5 nm the most intense. In our experiments laser beams with tens (or hundreds) of mW at the outlet of the laser cavity are used, as is typical in photothermal experiments. The laser beam has a diameter of approximately 2 mm at the exit. The beam intensity is modulated by an acousto-optic modulator (AA.MP MT80-A1-VIS). The modulation efficiency of the optical device is directly associated with the size of the illuminated region of the modulator crystal. The smaller the illuminated area, the greater the range of modulation frequencies obtained in the intensity of the beam exiting the modulator.

Thus, to reduce the diameter of the heating laser of the modulator, this focal point is positioned on a set of convergent lenses. After crossing the modulator, the laser beam passes through a diaphragm. The role of this element is to select only one of the beam diffraction orders. In general the first order diffraction is used, taking care to maximize power in that order. This is done by setting up the modulator on a positioning system having five degrees of freedom: three translational and two rotational. The beam is shifted to a dichroic mirror, with which it is finally focused on the sample surface through a metallurgical microscope (Olympus BH2-A) objective. Before entering the microscope, the laser beam is expanded to cover the entire ocular lens of the microscope; with this procedure, only the central area of the Gaussian beam passes through the ocular. In all cases we consider only normal incidence.

The microscope has 5 objective lenses with which we can define the diameter of the beam on the sample surface (Table 2.1). The beam radius is given by [59].

$$r = \frac{1{,}22\lambda}{2\ N.A} \qquad (2.1)$$

where λ is the laser wavelength and the numerical aperture of objective lens is N.A. In the above expression, we can easily find the following beam laser for the case $\lambda_{b1} = 514.5\ nm$, & $\lambda_{b2} = 488\ nm$ that lines commonly used in the experiments:

**Table 2.1**. Radius of pump beam and probe beam (eq 2.1). In function of the objective lens used in the microscope. The radius effective also shown.

| Magnification of the objective lens | N.A | Pump beam radius at $\lambda_{b1} = 514.5\ nm$ $r_{b1}(\mu m)$ | Pump beam radius at $\lambda_{b2} = 488\ nm$ $r_{b2}(\mu m)$ | Probe beam radius at $\lambda_p = 670\ nm$ $r_p\ (\mu m)$ | Effective Radius at $\lambda_{b1} = 514.5\ nm$ $r_{ef} = \sqrt{r_b^2 + r_p^2}$ $r_{ef}(\mu m)$ | Effective Radius* at $\lambda_{b2} = 488\ nm$ $r_{ef} = \sqrt{r_b^2 + r_p^2}$ $r_{ef}(\mu m)$ |
|---|---|---|---|---|---|---|
| **5X** | 0.10 | 3.14 | 2.98 | 4.09 | 5.16 | 5.06 |
| **10X** | 0.25 | 1.15 | 1.95 | 1.63 | 2.00 | 2.55 |
| **20X** | 0.40 | 0.79 | 1.22 | 1.02 | 1.29 | 1.59 |
| **50X** | 0.60 | 0.52 | 0.81 | 0.68 | 0.86 | 1.06 |
| **50X** | 0.75 | 0.41 | 0.65 | 0.54 | 0.68 | 0.85 |

The effective radius of the pump and probe beams obtained with the different microscope objectives. The effective radius, $\boldsymbol{r_{ef}}$ is a property that comes from the convolution product of two Gaussian functions in space, with $\boldsymbol{r_{b1}}$& $\boldsymbol{r_{b2}}$ and $\boldsymbol{r_p}$ radius. Functions have translational symmetry, so that the result is equivalent to one spatially point, while the other having an effective radius given by $\boldsymbol{r_{ef}}$.

The $Ar^+$ laser has a function of heating the sample (pump laser). Because this laser is modulated in intensity, the temperature in the sample will have a modulated component due to light absorption.

The beam modulation frequency is controlled by a function generator (Phillips PM5139, 0.1 mHz - 20 MHz). To analyze the temperature variation (continuous and modulated components) we used a laser-diode (COHERENT, 10 mW) continuously emitting at 670 nm; this laser (probe) is coupled to the input of a photographic microscope. After passing through a beam splitter cube, the retarding λ / 4 filter (670 nm) and the dichroic mirror, the probe beam is focused on the sample surface.

After being reflected by the sample, the probe beam passes again the λ / 4 filter. Having now turned its polarization vector 90 degrees, the beam is deflected by the splitter cube. The use of this optical element has two advantages: laser protection, preventing the beam is reflected back to its own cavity, and diverts it to a photodetector (NEW FOCUS 1801). The probe beam is carefully positioned so that its diameter on the photodetector surface is smaller than the area of the photocell. This is done with the aid of a lens positioned convergent before the photodetector. This treatment is important to avoid that small variation in position and intensity of this beam. We are interested only in induced modulation on the probe beam, or the variation of the reflectance. The output signal of the photodiode is analyzed by a synchronous lock in amplifier (SR830). To scan the sample surface with the pump beam, and probe laser we make use of a micro positioning system to x-y (Motion Controller ESP300 Newport).

The experiments are automated, and a microcomputer controls the translation system, the function generator and reads the two amplifier channels via the GPIB card, storing the continuous ($DC$) and alternating component ($AC$) signal. The $dc$ component, $S_{dc}$, is proportional to the reflectivity $R$ in the sample at a certain reference temperature $T$, while the modulated component, $S_{ac}$, of the reflectivity $\Delta R$ is proportional to the excursion $\Delta T$ temperature around the mean reference temperature $T$. By measuring both components, the experimental value of $\Delta R / R$ can be obtained, as

$$\frac{\Delta R}{R} = \frac{S_{ac}}{S_{dc}} = \frac{1}{R}\frac{\partial R}{\partial T}\Delta T. \tag{2.2}$$

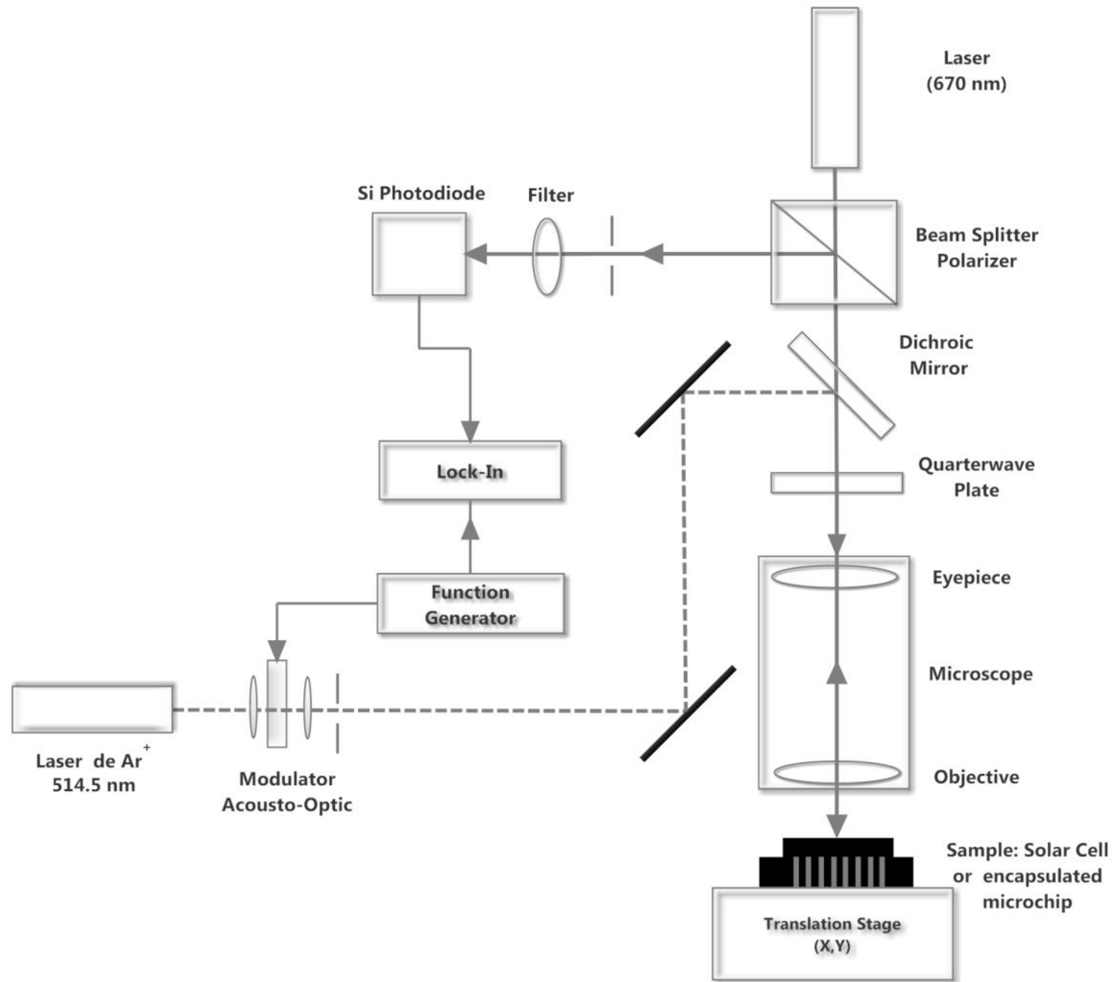


**Fig. 2.2:** Scheme of the experimental set-up for photothermal reflectance microscopy using an $Ar^+$ laser as an excitation

## *2.3.2. The sample as a source of excitation by Joule Heating. (Thermoreflectance).*

For studying electronic devices in operation, the excitation was done by modulated current/voltage applied to the circuit. The non-modulated probe laser beam scans the sample surface to record its thermal image. The experimental arrangement used for obtaining the images is illustrated in Fig. 2.3. A probe beam, coming from a 670 nm laser diode, enters a commercial microscope through its photograph eyepiece, and is focused on the sample surface after passing the objective.

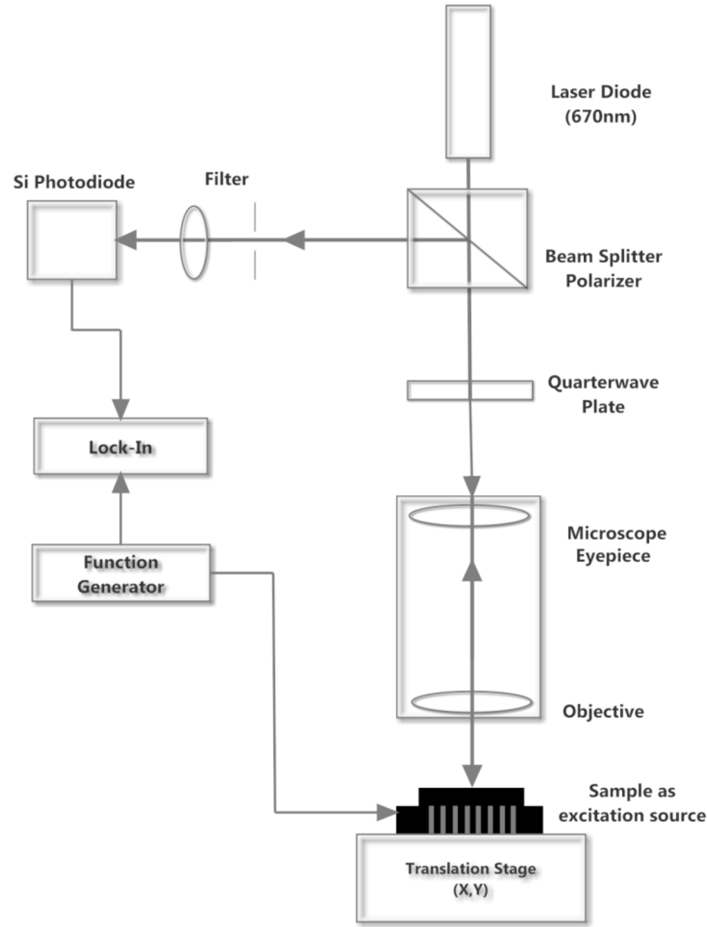


**Fig. 2.3**: Scheme of the experimental set-up for photothermal reflectance microscopy in microelectronic devices, using the sample as excitation source.

The spot diameter is about 1.0 $\mu m$ when using a numerical aperture of 0.75 (50 x objective). The beam is reflected back by surface of the sample and desviated in the direction of a Si photodiode by using a $\lambda/4$ plate combined with a polarizing beam splitter cube. The sample is mounted on an x-y translation stage of step-size 0.1$\mu m$. The modulated voltage applied to the sample has the form $V(t) = (V_0/2)[1 + \sin(2\pi f t)]$, with $f$ varying from a hertz to a hundred kilohertz. The reflected probe beam is intensity modulated as well due to the current flow and voltage modulations. For the particular waveform of the applied voltage above, there is joule dissipation at the frequency $f$ and at $2f$ as well.

The output signal from the Si detector is lock-in analyzed (reference in phase with the $AC$ driving potential) and its $DC$ component is used to normalize the lock-in signal, giving the experimental values of $\Delta R/R$, in the same way the output signal of the PZT detector is analyzed by another lock-in.

## 2.4 Combined Thermoacoustic and Thermoreflectance set-up.

Recently, we employed a lead zirconate titanate (PZT) sensor underneath the sample to characterize liquids by scanning a pump beam tens/hundreds of micrometers along the upper surface of an absorbing material, using the experimental set-up described in section 2.2 [19, 21]. In the mentioned work it has been demonstrated that the transducer is capable to detect the signal originated in one point of the sample surface without been affected but lateral heat diffusion effects or thermal wave reflections [58]. Using the same photoacoustic microscope, images of microelectronic circuits and solar cell structures have been obtained. Therefore, we decided to use an extended version of this setup, combined with thermoreflectance, for imaging. We use the conventional thermoreflectance microscopy to correlate with the thermal/acoustic detected signal by the PZT sensor. This Set-Up can see in the illustrated Fig. 2.4.

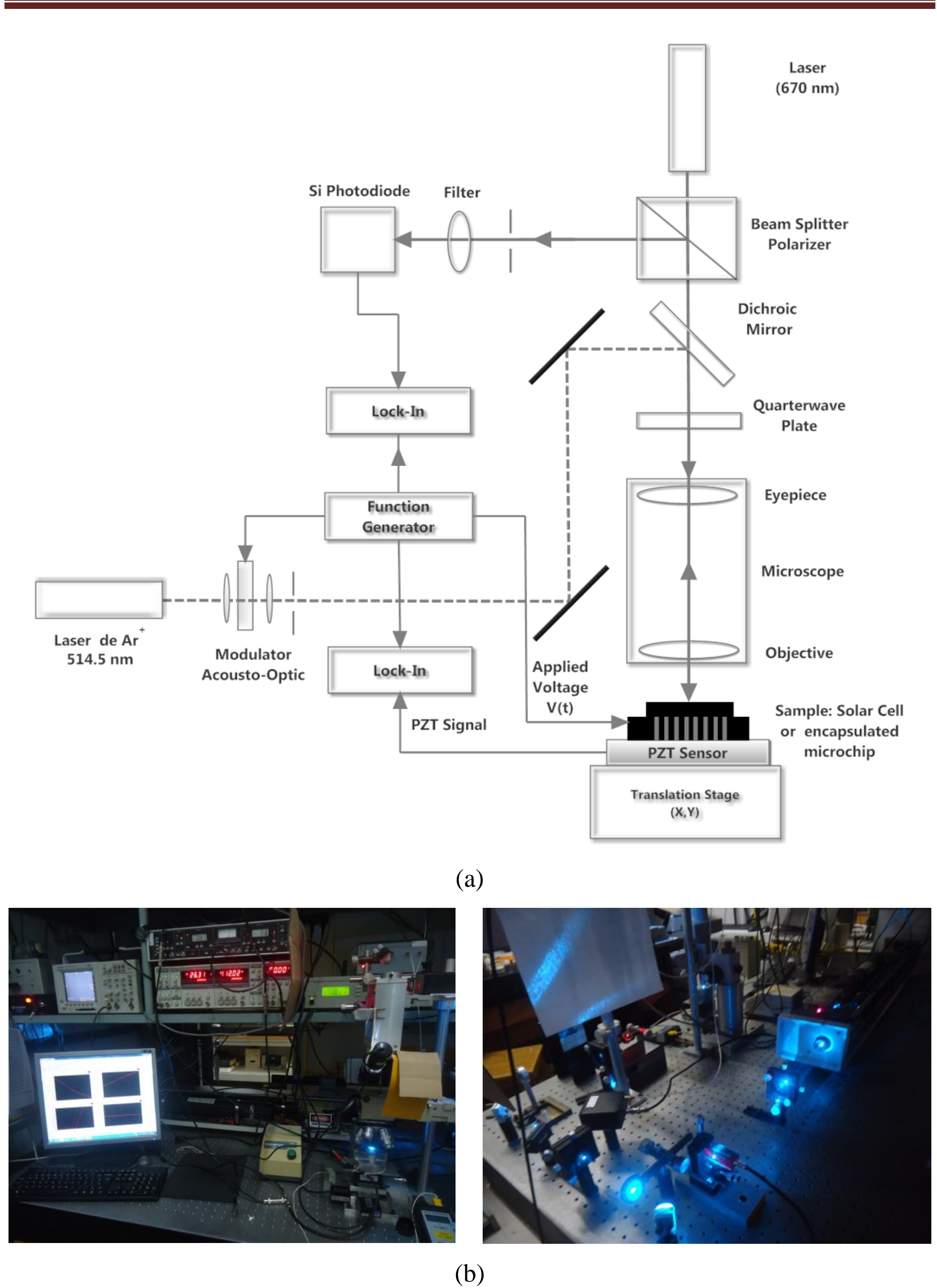


(a)

(b)

**Fig. 2.4**: Experimental arrangement mounted of PAM (thermoreflectance and thermoacoustic). (a) Scheme experimental of the combined thermoreflectance with thermoacoustic set-up. (b) Photographs of experimental setup.

# SCANNING PHOTOACOUSTIC MICROSCOPY OF A SMART CARD.

CHAPTER 3

## 3.1 Imaging of a Smart Card Chip (SCC).

The experimental arrangement used to obtain the photoacoustic images with piezoelectric detection is shown in the Fig. 2.1(a), of the chapter two. The sample used was a SCC, due of its convenient size and architecture shown in Fig. 3.1. Applying the PAM we can detect characteristics below the surface of the chip in a non-destructive way.

## 3.2 General considerations.

A smart card, chip card, or integrated circuit card (ICC), is any pocket-sized card with embedded integrated circuits which can process data. This implies that it can receive input which is processed by way of the ICC applications and delivered as an output.

The inside of a smart card usually contains an embedded microprocessor. The microprocessor is under a gold contact pad on one side of the card. Smarts cards may have up to 8 kilobytes of RAM, 346 kilobytes of ROM, 256 kilobytes of programmable ROM, and a 16-bit microprocessor. The smart card uses a serial interface and receives its power from external sources like a card read.

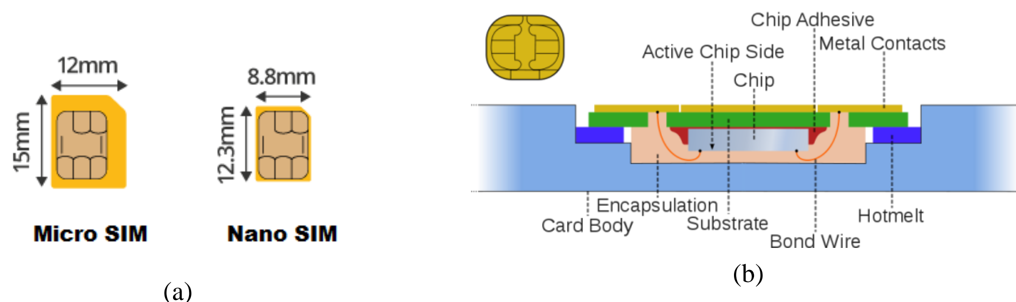


**Fig. 3.1:** Architecture of SCC. a) SCC types and dimensions a) Schema of SCC structure and packaging

***Uses of Smart cards***

The most common applications of Smart cards are:

- **Stored Value** – The primary use of smart cards is stored value, particularly loyalty programs that track and incentivize repeat customers. Stored value is more convenient and safer than cash.
- **Securing Information** – In addition to information security, smart cards achieve greater physical security of services and equipment, because the card restricts access to all but the authorized user.
- **E-Commerce**– Smart cards make it easy for consumers to securely store information and cash for purchasing. The card can carry personal account, credit and buying preference information that can be accessed with a mouse click instead of filling out forms.
- **Personal Finance** – Customers can use secure smart cards for fast, 24-hour electronic funds transfers over the internet
- **Health Care** – Rapid identification of patients; improved treatment. A convenient way to carry data between systems or to sites without systems. Reduction of records maintenance costs.

***Types of smart cards.***

Contact smart card readers are used as a communications medium between the smart card and a host, e.g. a computer, a point of sale terminal, or a mobile telephone. Since the chips in the financial cards are the same as those used for mobile phone Subscriber Identity Module (SIM) cards, just programmed differently and embedded in a different shaped piece of PVC, the chip manufacturers are building to the more demanding GSM/3G standards.

***Smart card pin out showing in Fig. 3.2***

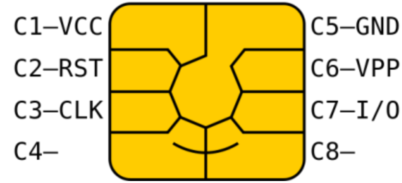


**Fig. 3.2**: A smart card pinout

- VCC: Power supply input
- RST: Used itself or in combination with an internal reset control circuit.
- CLK: Clocking or timing signal
- GND : Ground
- I/O: Input or Output for serial data to the integrated circuit inside the card.
- VPP : Programming voltage input

The use of the two remaining contacts are defined in the appropriate application standards. Figure 3.3 shows the SCC card studied here. In the upper part of the figure it is showed a photograph of the card and the lower part shows the rear side of the card with the cover removed to improve the quality of the obtained photoacoustic images. The chip attached to the PZT sensor is shown in part (b). Note that the removed cover is substituted by the thermal past (white region in Fig. 3.3 (b)).

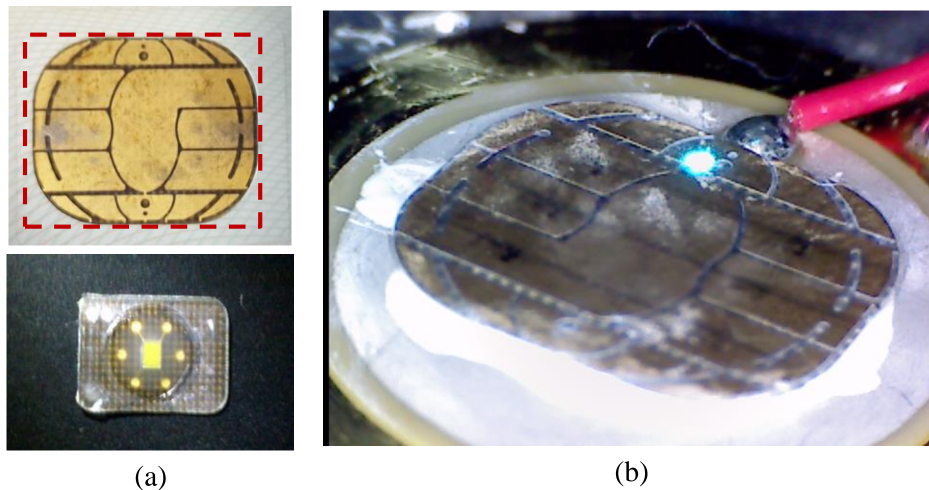

(a) (b)

**Fig. 3.3**: Optical images of SCC used. (a) At the top shown the front face of SCC and in the bottom shown the rear face, the back cover was removed. (The red dotted line is the scanned area). (b) SCC mounted on the PZT detector. The rear cover was removed and replaced with thermal paste.

## 3.3. Results and Discussion.

The figures 3.4 (a) and (b) show the amplitude and phase maps respectively of the area (14 mm x 12 mm) indicated in Fig. 3.3 (a), where each pixel corresponds to 120 μm x 120 μm. The modulation frequency used was 100 Hz. The sample´s rear side is attached to the PZT sensor and it is illuminated at its front surface. It can be shown that most subsuperficial features of the SCC card showed in Fig. 3.4. (b), were resolved in these images. The amplitude image is more noisy because it is influenced not only by the thermal parameters of the sample (as the phase image is), but also by the optical parameters (note that in obtaining Eq. (1.7) of the Chapter 1) it has been assumed an ideal sample with superficial optical absorption, but for a non-ideal sample the amplitude becomes affected by optical parameters such as optical absorption and reflection coefficients [22]). Parts (b) and (c) show the In-phase and Quadrature images respectively, calculated using the amplitude and phase values. They are obtained in order to apply the phase separation method described in Chapter 1, as will be shown later.

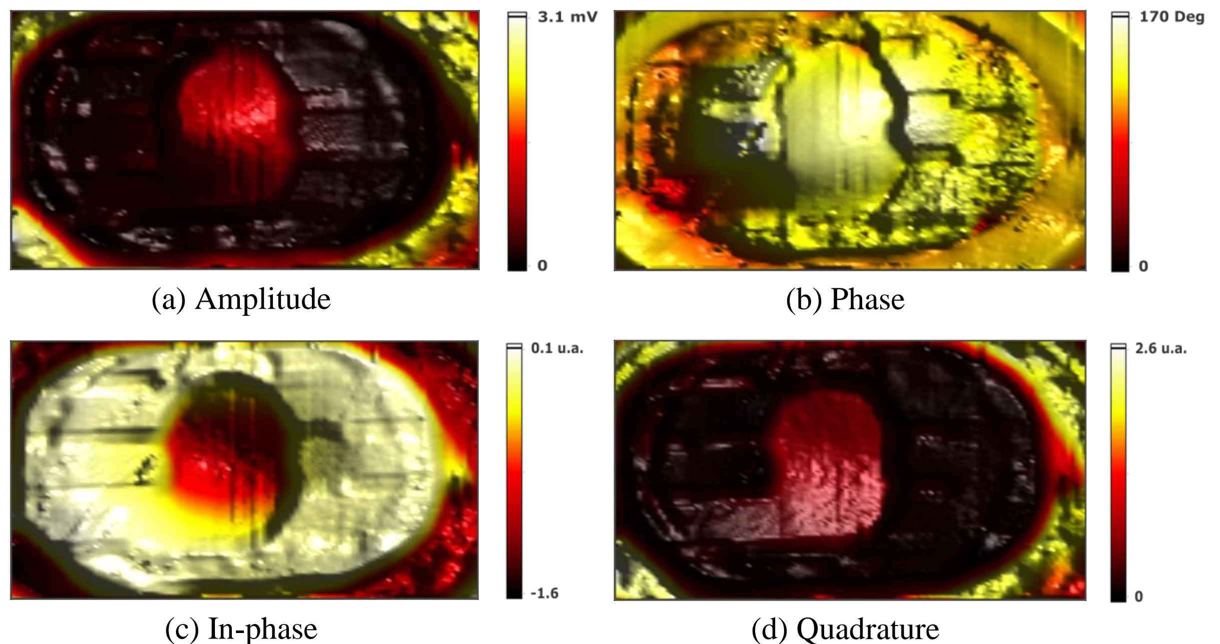


(a) Amplitude (b) Phase

(c) In-phase (d) Quadrature

**Fig. 3.4**: Images obtained from an SCC using PAM with piezoelectric detection. Laser hits in the front surface of the SCC, while the PZT is attached at the SCC rear face. (a) PAM amplitude image. (b) PAM phase image. (c) PAM in-phase image. (d) PAM quadrature.

Similar pictures are presented in Fig. 3.5 for the sample shown in the lower part of Fig. 3.3. (a). The face of the uncapped sample showed in that figure is attached to the PZT sensor and illumination took place at the opposite side.

Using the In-phase and quadrature images showed in figures 3.4 and 3.5 the phase separation method was applied. The results for five characteristic phase angles are shown in Fig. 3.6. It is well known that this method is useful to resolve subsuperficial features of a sample. Here we can see that at 324 degrees noise is strongly removed from the original amplitude images, and that the images become very similar to those showed by the former In-phase components. This is an awaited result that can be explained as follows: The signal obtained from the lock-in amplifier is divided into amplitude $(A)$ and phase $(\varphi)$, which can be represented by two components:

$$X = A\cos\varphi \quad \& \quad Y = A\sin\varphi \qquad (3.1)$$

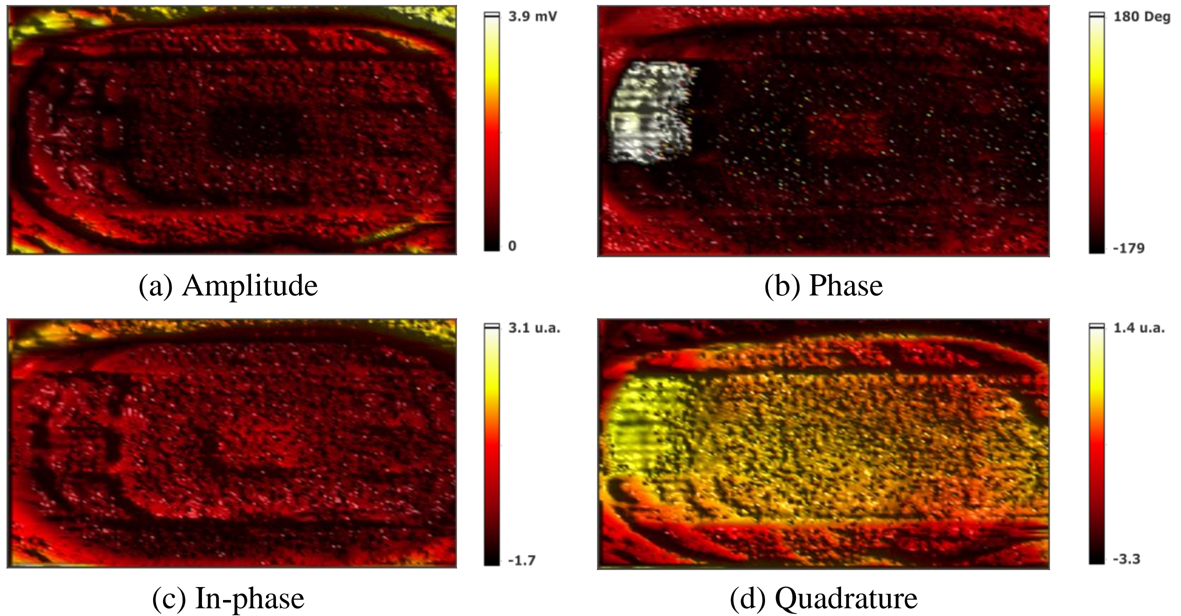


(a) Amplitude (b) Phase

(c) In-phase (d) Quadrature

**Fig. 3.5**: Images obtained from an SCC using PAM with piezoelectric detection. Laser hits in the back surface of the SCC, while the PZT is attached to the SCC front face. (a) PAM amplitude image. (b) PAM phase image. (c) PAM in-phase Image. (d) PAM quadrature.

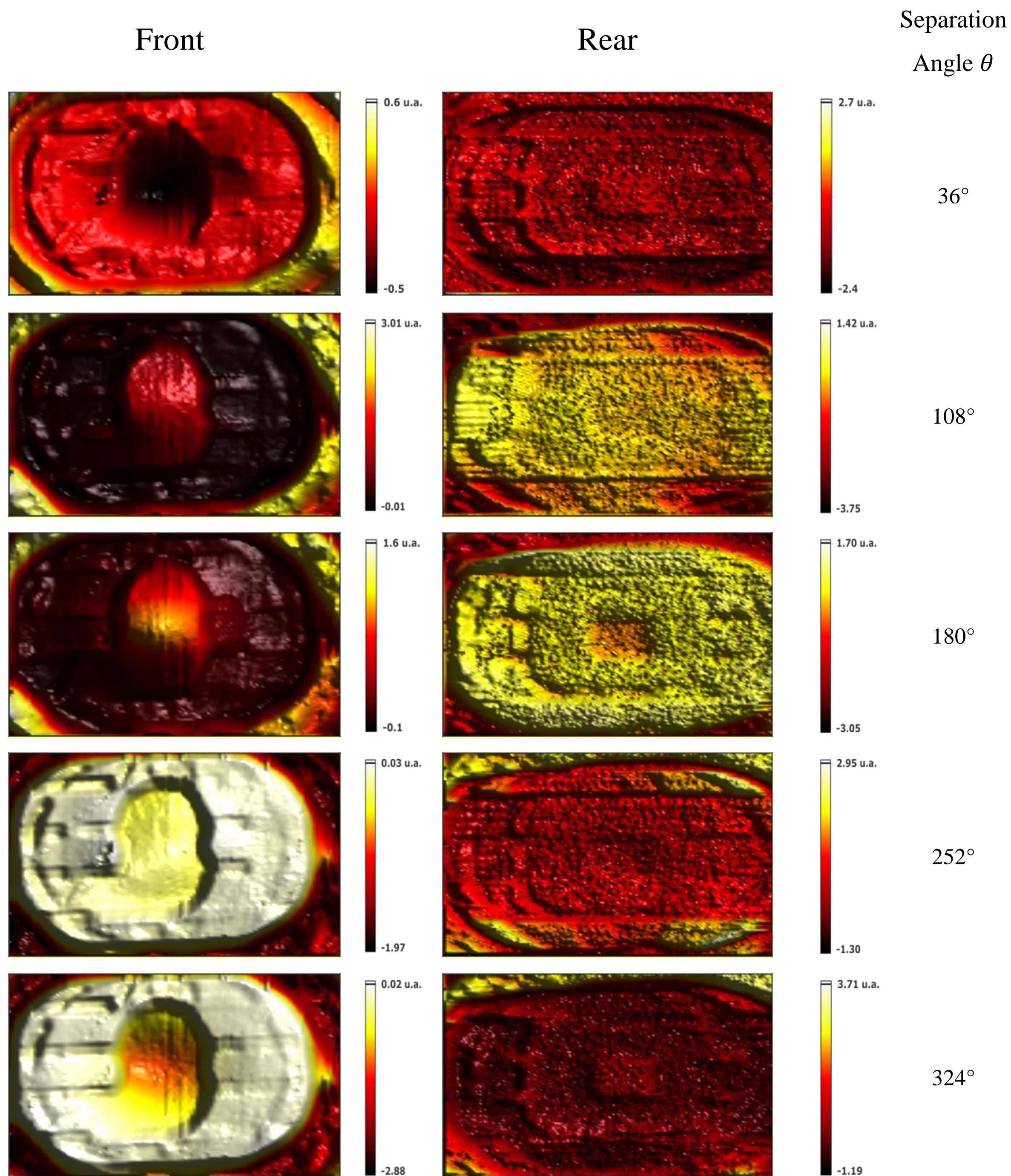


**Fig. 3.6:** Images obtained through of Phase-Resolved method using PAM. In each image, exist a separation between angles of 36 degrees.

These two quantities represent the signal as a vector relative to the reference modulation given by the lock-in. $X$ is called the component “in-phase” and $Y$ is called the component in “quadrature”. This is because when $\varphi = 0$, we have only the component in $X$, since the component in quadrature is $Y = 0$.

One way to find the component in phase is to maximize the signal photo-piezoelectric from the lock-in amplifier, and not from the source of radiation (laser). But by adjusting the phase of the reference signal, the signal component in phase will be proportional to the amplitude of the photo-piezoelectric signal. This procedure can be quite lengthy, so that the phase separation method becomes a useful tool for analyzing photothermal images.

# Combined PRM and PAM set-up, for imaging unbiased in solar cells and non-encapsulated microelectronics chip.

CHAPTER 4

The experimental arrangement used to obtain the photoacoustic and reflectance images is shown in Fig. 2.2 of chapter 2. The sample used was a naked Solar Cells Assembly (SCA) and non-encapsulated Chip.

## 4.1 General considerations of Solar Cell Assembly SCA.

The experimental results were obtained through a photovoltaic cell used in satellites solar panels. The samples were supplied by the Brazilian Aerospace Research National Institute (Instituto Nacional de Pesquisas Espaciais, INPE) [60]. The SCA is a multilayer composite system showed schematically in Fig. 4.1 (a). It is composed by an electrical interconnector soldered on the front contacts (1), an adhesive layer between a cover glass (1) and the active surface of the naked solar cell (3). This glass slide is used primarily to protect the solar cell against particle radiation normally found in space. The Metallized contacts on the (active) front of the solar cell is welded with electrical contact (interconnector). Fig. 4.1. (b) shows typical dimensions.

One of the reasons for imaging SCAs is the enormous temperature gradient in the orbital environment, causing bubbles that can expand, causing damage to the SCA structure. Cracks in the inner layers of the panel of the SCA caused by vibrations during testing can be identified by application of this technique. One of the key proposals of this study is to obtain images of a naked solar cell (see Fig. 4.2 (a)), because its main construction is formed by three thin films, as shown in Fig. 4.2 (b).

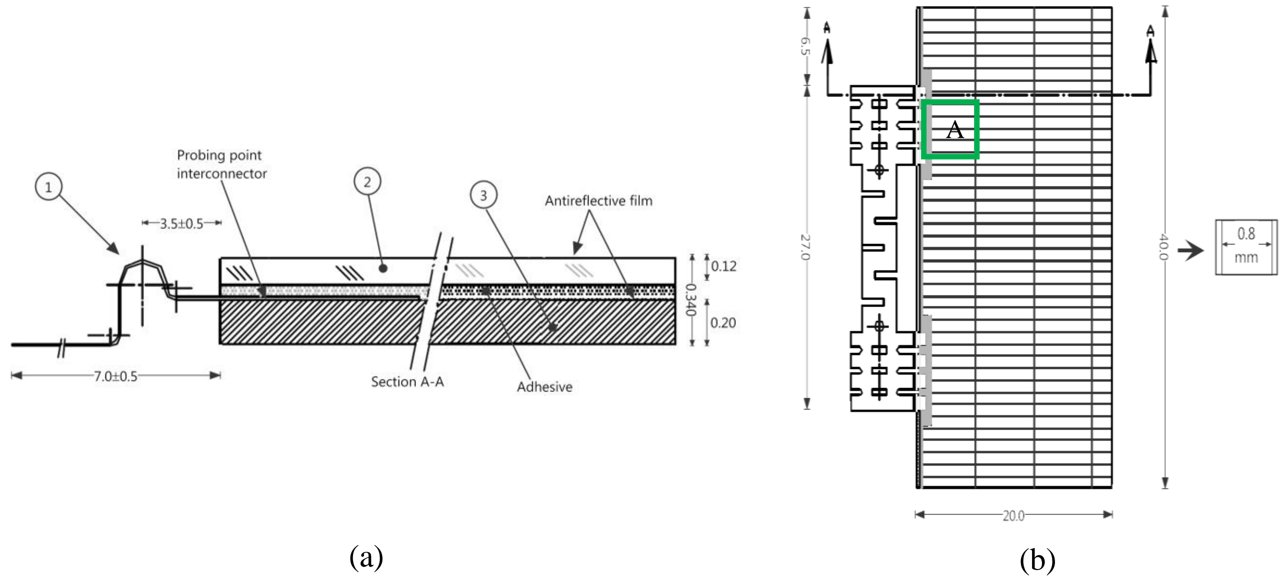


(a) (b)

**Fig. 4.1:** Architecture of a SCA in detail. (a) Side view of a SCA (not in scale) with an anti-reflective film / adhesive and glass-corning / anti-reflective film. The marked area ($A$) was selected because of the proximity that it has with the points of welding (b) Front view. Each separation between two conductive tracks of silver, it has an extension of 0.8 mm.

**Table 5.1** Shows the physical characteristics of the naked SCA, which is composed of a silicon solar cell (20mm x40 mm x 0.020mm) covered with anti-reflective layer [74].

| Number | Type | Defect |
|---|---|---|
| 001126 | Naked Solar Cell / Flight Model 2 | No defect |

**Table 5.1.** Sample description.

For PRM measurement a laser diode operating at 632.8 nm was used as a probe beam, which has a spot diameter of about 1.5µm. An $Ar^{+}$ laser of 488 nm wavelength was used as excitation, with a spot diameter of about 2.0 µm. The power at the laser output was 400 mW. Both laser beams were focused on the same point on the sample with powers about 0.1 mW (probe) and a few miliwatts (excitation). The scanned area is shown in Fig. 4.2 (a) with dashed lines. The sample is attached at its rear side to a PZT sensor using thermal past in order to record, in the same set-up, both the MPR and PAM images. The scanning was done with a 45.0 $\mu m$ step.

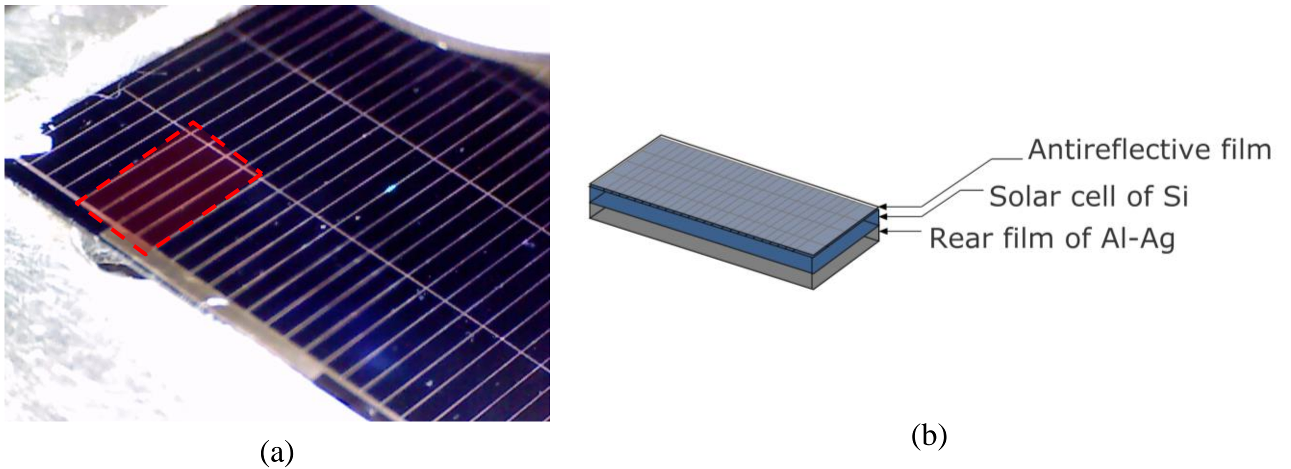


(a) (b)

**Fig. 4.2:** Optical image and description of naked SCA. (a) Side view of the naked solar cell, the dotted area is the analysis area (7.65 mm x 2.9 μm). The surface has a grid of metallic contacts covered by an anti-reflective layer. (b) Is the cross-section of a naked SCA used (Out of scale), where it shows the different layers between the back film of Al-Ag and the antireflective film.

### *4.1.1 Results and discussion of the SCA.*

In previous sections we showed the imaging possibilities of both PRM and PAM techniques. Here we show an example of the application of both techniques for imaging the same object. In Fig. 4.3 we show the images obtained in the PRM and PAM modes to of the naked SSA showing that PZT detection is capable to reproduce the same superficial features of the sample as the PRM technique does. Note that, as mentioned in Chapter 1, the disturbance $\Delta R$ of the static reflectivity $R$ is proportional to the $S_{ac}$ component of the modulation frequency $f$, while the $S_{DC}$ component (reflecting a pure optical response) is proportional to $R$ itself.

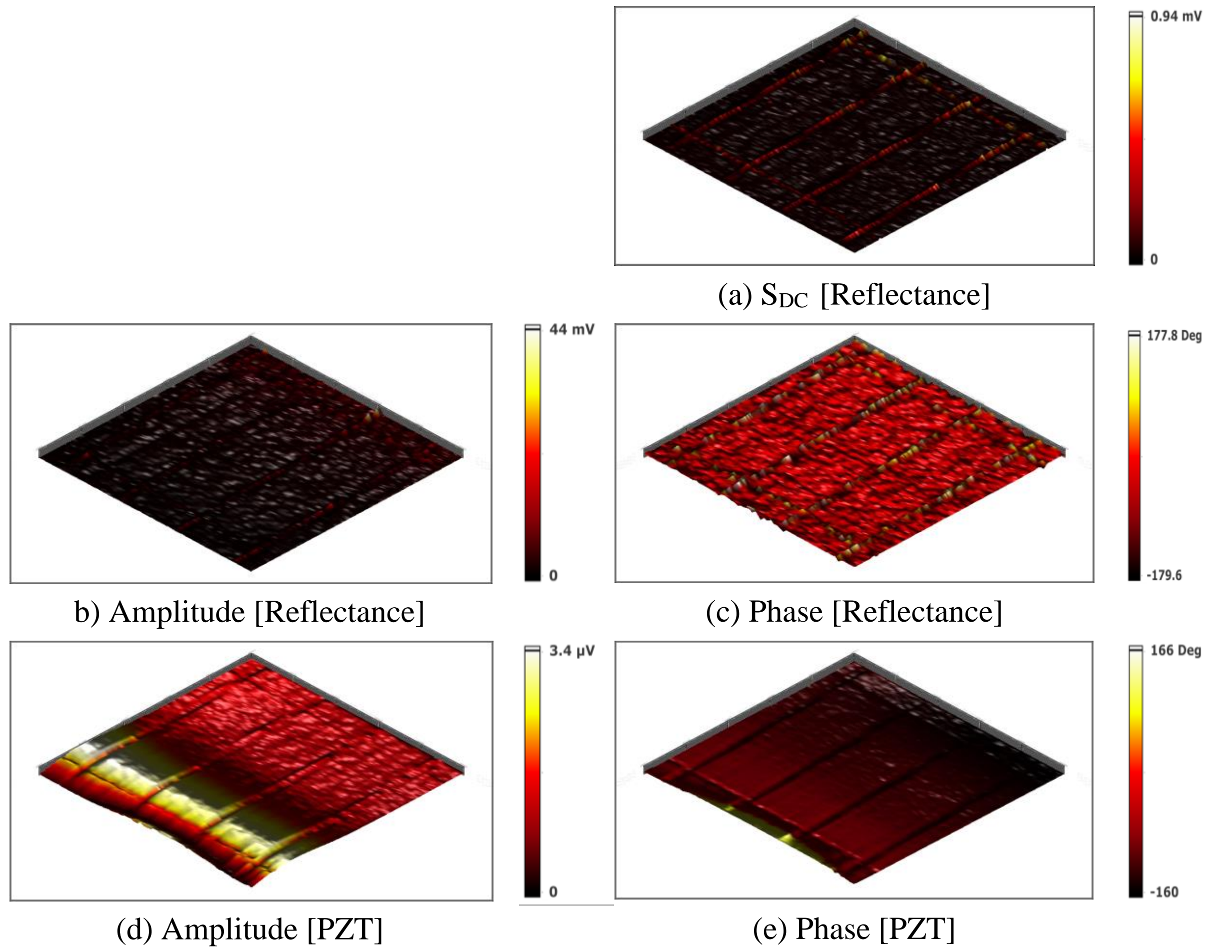


(a) $S_{DC}$ [Reflectance]

b) Amplitude [Reflectance]

(c) Phase [Reflectance]

(d) Amplitude [PZT]

(e) Phase [PZT]

**Fig. 4.3:** Images of a naked SCA using PRM and PAM in the grid section. (a) DC PRM ($S_{DC}$) image, (b) PRM amplitude image (c) PRM phase image. (d) PAM amplitude image (e) PAM phase image.

From the images obtained by the PZT it can be seen that the extreme regions at the left of the solar cell reveal certain inclinations or curvature in the wedge shape, similar to those discussed in the analysis accomplished by the works of Costa [60] and Batista [61] in multilayer systems. These are promissory results that can allow to detect problems in some areas of adhesion between films.

Another example of the possibilities of this combined set-up is the following. An area of 330 μm x 300 μm of the front surface of a solar cell is shown in Fig. 4.4 (a) (optical image). Fig. 4.4 (b) is the DC PRM image. The vertical structure of the solar cell (naked, without cover glass protection), consists of the silicon cell itself (200 μm), the Ti/Pd/Ag grid used for the front electric contact, and the rear Al/Ag contact layer. The cross form in the picture is part of the front metallic grid contact. Figure 4.4(c) represents the thermoreflectance amplitude map using f = 100 Hz as modulation frequency of the pump laser beam (514.5 nm, 1.6μm in diameter).

The image clearly contrasts the Ti/Pd/Ag grid, as expected. Phase map (part (d) of the figure) corroborates the same geometry. Figures 4.4 (e) and (f) shows the amplitude and the phase of the thermoacoustic image, detected by the PZT simultaneously with the reflectance signal by using a second lock-in amplifier. It has to be observed that the PZT signal is transmitted across the sample thickness (~ 200 μm), once the heat generation takes place mostly at the front surface of the Si cell.

The thermal diffusion length in Si (thermal diffusivity $\alpha Si=0.9$ $cm^2/s$ [18]) is $\mu=(\alpha/\pi f)^{1/2}=535$ μm at f = 100 Hz. It means that a significant amount of modulated heat reaches the PZT sensor in this case, thus generating signal through the pyroelectric effect, but also the piezoelectric contribution can be present.

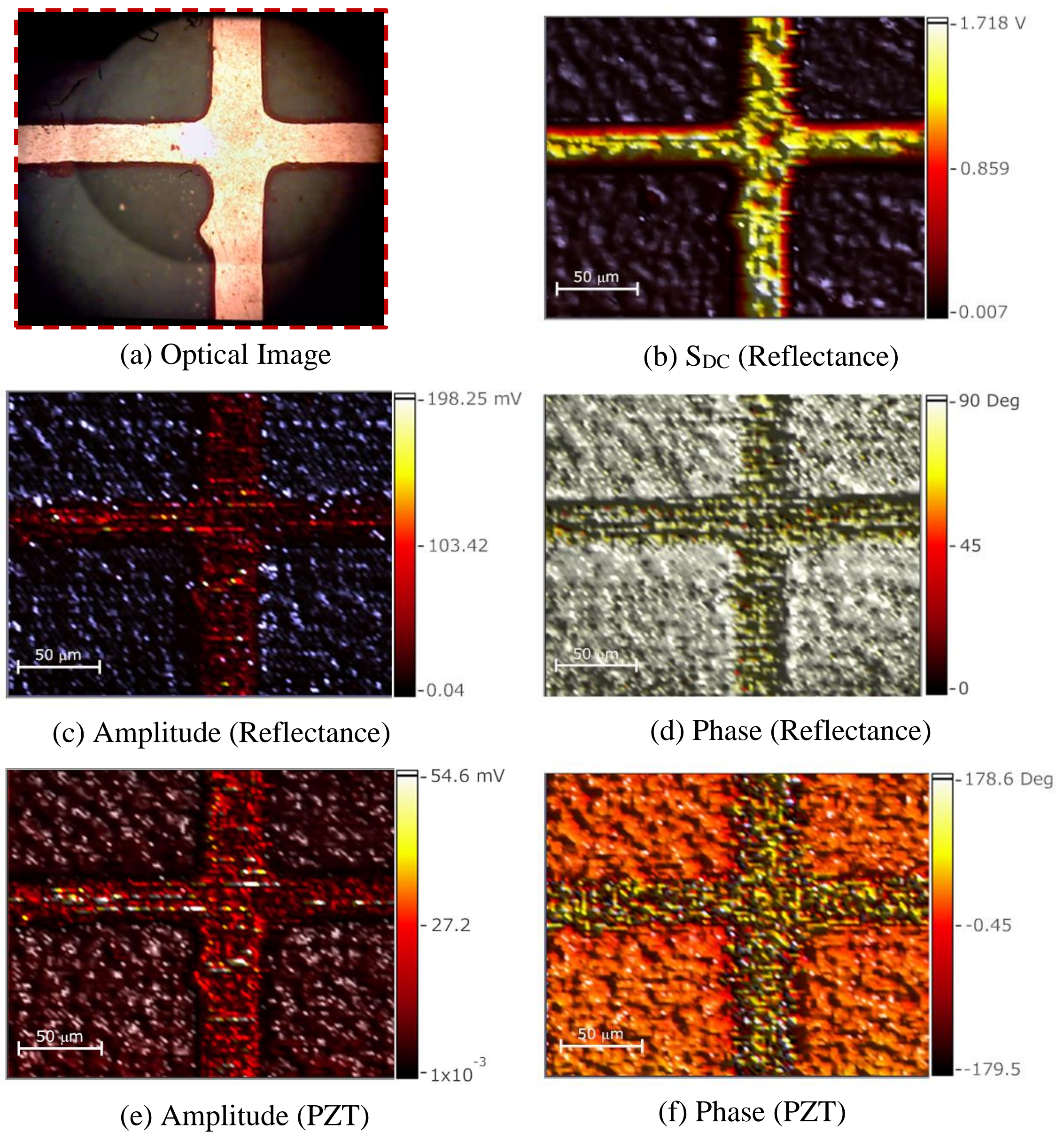


(a) Optical Image (b) $S_{DC}$ (Reflectance)

(c) Amplitude (Reflectance) (d) Phase (Reflectance)

(e) Amplitude (PZT) (f) Phase (PZT)

**Fig. 4.4:** Images of a naked SCA using PRM and PAM in the metallic contact (cross form). (a) Optical photograph of the front surface of a naked solar cell (330 µm x 300 µm) showing the metallic contact (cross form) and the red dotted line is the scanned area. Pump laser beam: 514.5 nm, 1.6 µm in diameter, 400 mW power at the laser output, modulated at f = 100 Hz. Probe beam: 632.8 nm, 2.0 µm in diameter. (b) PRM DC Image map (c) PRM amplitude map; (d) PRM phase map (e) PAM amplitude map on the metallic line) and (f) PAM phase map maps.

Pump laser beam: 514.5 nm, 1.6 μm in diameter, 400 mW power at the laser output, modulated at f = 100 Hz. Probe beam: 632.8 nm, 2.0 μm in diameter.

## 4.2 Thick film technology (TFT). Imaging on chip unencapsulated

Another example to show the possibilities of the combined PRM and PAM set-up is the imaging of non-encapsulated circuits.

### *4.2.1 General considerations of the TFT on chip.*

Thick film circuits are fabricated by screen printing conductive, resistive, and insulating materials in the form of a viscous paste onto a ceramic substrate. The printed film is dried to remove volatile components and exposed to an elevated temperature to activate the adhesion mechanism that adheres the film to the substrate. In this manner, by depositing successive layers, multilayer interconnection structures can be formed that may contain integrated resistors, capacitors, or inductors etc.

Printed substrates are of considerable use in aggressive environments and in cases where classical materials fail. They are applied in automotive and aerospace industry, medical industry, LED illumination, power electronics, hybrid microelectronics, microwave circuits, sensors, electronic components, etc. Thin film technology involves deposition of individual molecules or atoms. Thick film technology involves deposition of particles.

The lithography process must be realized in a special room named clean room. The need for this clean room is due to the fact that the particles of dust of the air can settle on the surface of the semiconductor and the lithographic masks causing defects in the devices. In a clean room, there is controlled exactly the entire number of particles of dust by volume unit.

Electrostatic discharge is the main problem in several steps of the construction process, encapsulation and use of a device. Conventional degradation research methods are based on the electrical characteristics of devices. Threshold voltage measurements and leakage current, for example, allow monitoring of degradation during testing. This type of measure takes into account the overall damage to the structure and it is not possible to reveal the exact position of the damage or its spatial extent.

### *4.2.2 Results and discussion.*

Fig. 4.5 shows a photograph of a microelectronic non-encapsulated chip, named here Chip 01.

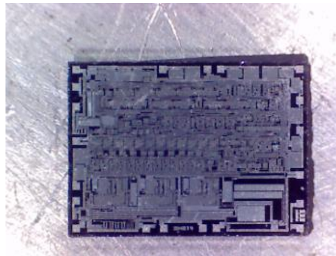

Chip 01

**Fig. 4.5:** Optical image of unencapsulated chip used to obtain images by PRM and PAM.

The figure 4.6 and shows the photothermal image taken at f= 100 Hz obtained in a small region of Chip 01, whose optical images is represented in part (a) of the figure.

These images show that PAM allows a better visualization of the circuit´s tracks than PRM, which has been established during the last years as a useful technique for imaging microelectronic circuits. These result was an inspiration to apply the same combined PAM and PRM setup for imaging biased microelectronic circuits, as will be shown in the next chapter.

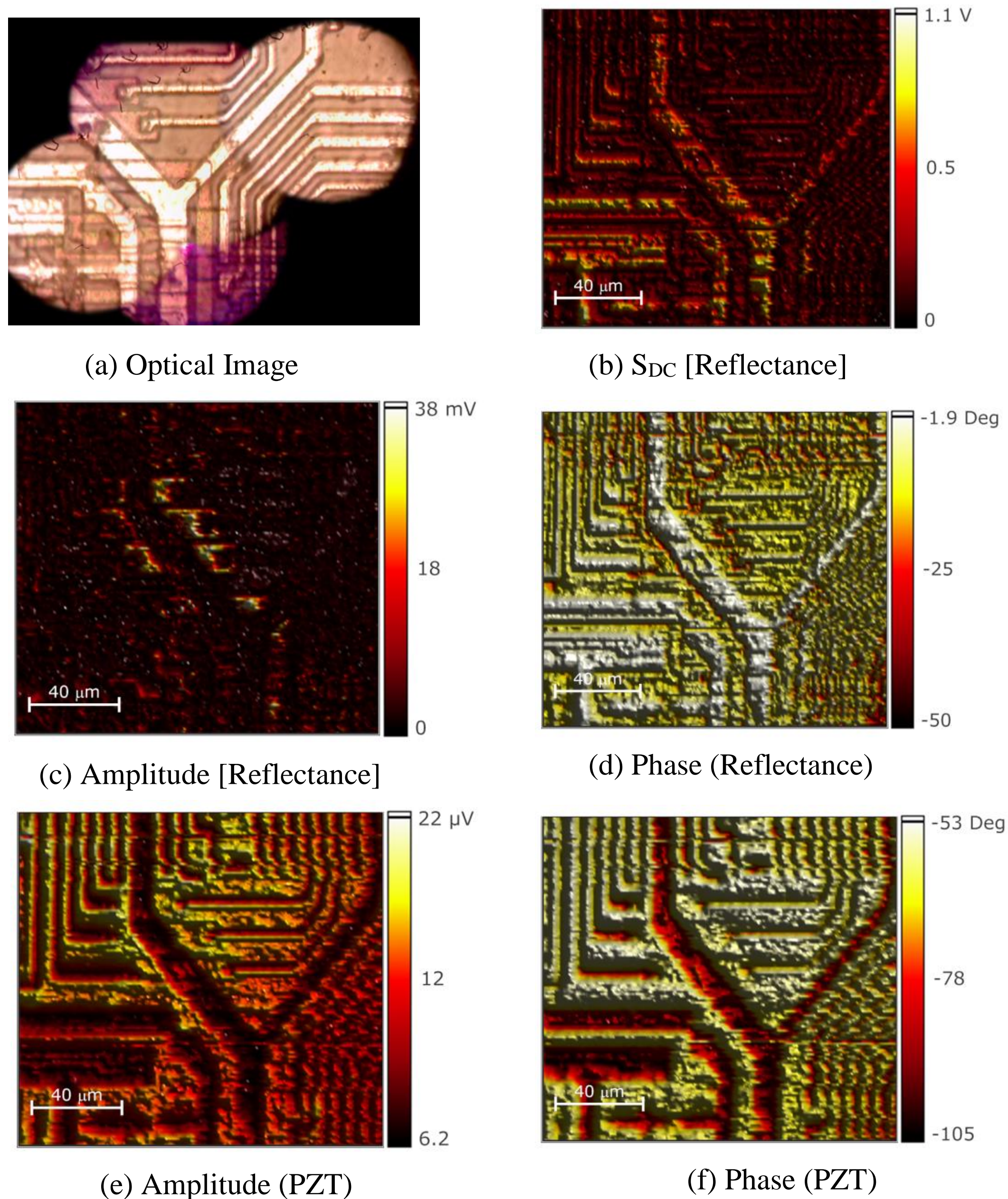


(a) Optical Image (b) $S_{DC}$ [Reflectance]

(c) Amplitude [Reflectance] (d) Phase (Reflectance)

(e) Amplitude (PZT) (f) Phase (PZT)

**Fig. 4.6:** Front surface images of a small region (200 µm x 151 µm) of an un-encapsulated chip-01 showing in the center a characteristic Y-shaped track (surface and subsurface tracks). (a) optical image, (b) PRM $S_{DC}$ image, (c) PRM amplitude map, (d) PRM phase map, (e) PAM amplitude map and (f) PAM phase map.

# Imaging of Biased Encapsulated Microelectronic circuits using a combined Thermoreflectance and Thermoacoustic set-up.

CHAPTER 5

## 5.1 Introduction.

In this section a combined thermoreflectance and thermoacoustic set-up described in the previous chapter is used for imaging biased microelectronic circuits. In particular, it was used with polycrystalline silicon resistive tracks grown on a monocrystalline Si substrate mounted on a test chip. Thermoreflectance images, obtained by scanning a probe laser beam on the sample surface, clearly show the regions periodically heated by Joule effect, which are associated to the electric current distribution in the circuit. Although the thermoacoustic signal, detected by a pyroelectric/piezoelectric sensor beneath the chip, also discloses the Joule contribution of the whole sample, additional information emerges when a non-modulated laser beam is focused on the sample surface in a raster scan mode allowing imaging of the sample.

## 5.2 Description of the test chip LACAM-02.

The test chips characterized here (Fig. 5.1), named LACAM02, were designed at the Laboratory of Characterization of Materials (LACAM) of the Institute of Microelectronics, of the Technological Centre for Computer Science – CTI, Campinas, SP, Brazil, and manufactured at the Centro Nacional de Microelectrónica CNM, Spain. This test chip has incorporated electronic devices (transistors, diodes, capacitors, etc.), as well as analog and digital circuits.

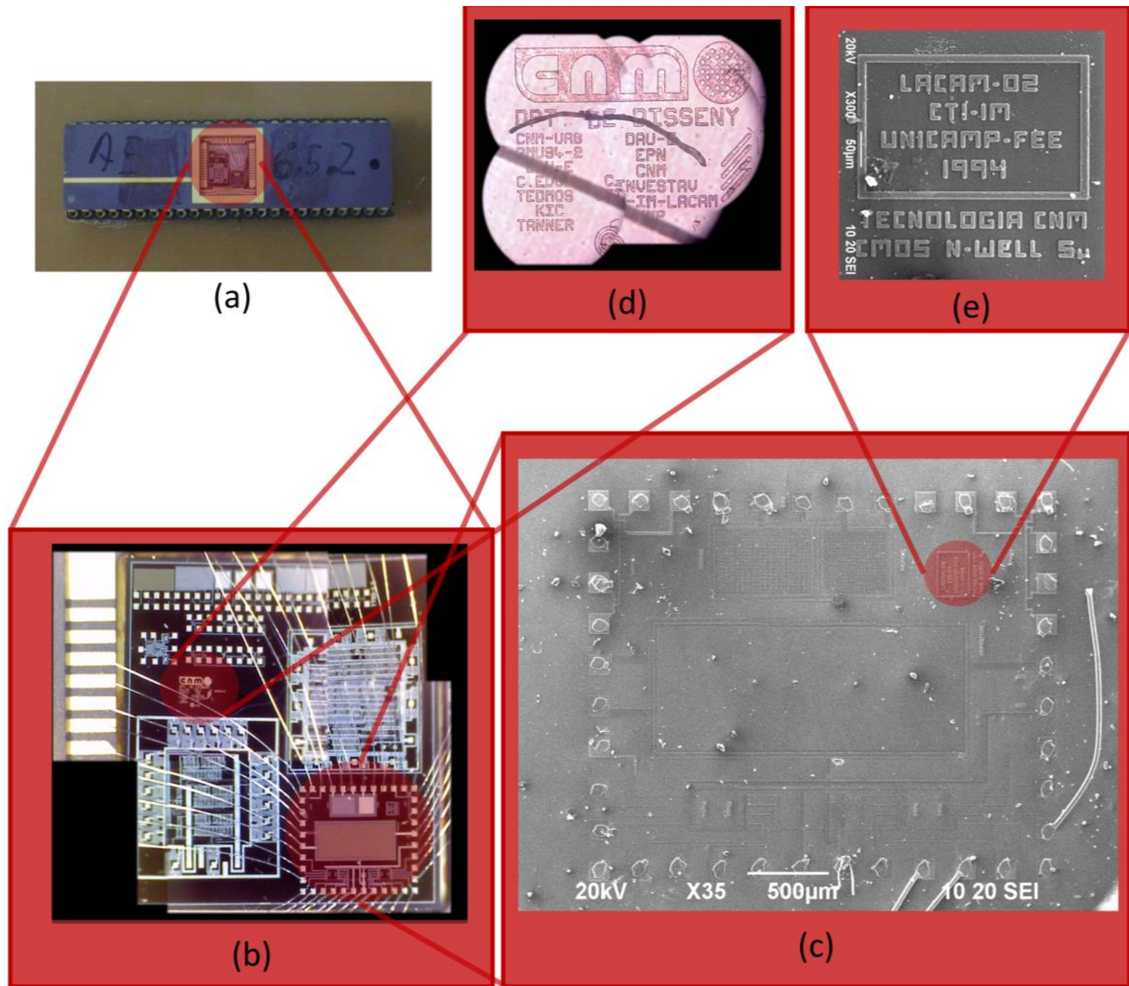


**Fig. 5.1:** Detailed images of the test chip. (a) Optical image of the encapsulated test chip. View from outside. (b) Approach of the wired area to polarize (Before removing the wires of gold). (c) Micrograph obtained by Scanning Electron Microscopy (SEM) of the test chip LACAM-02. It can be observed devices and structures to polarize (They had to remove the gold wires to observe it in the SEM). (d) Description of manufacturer. (e) Description of the technology used by the manufacturer.

The circuit shown in the Figure 5.1c includes the devices and structures showed in Fig. 5.2.

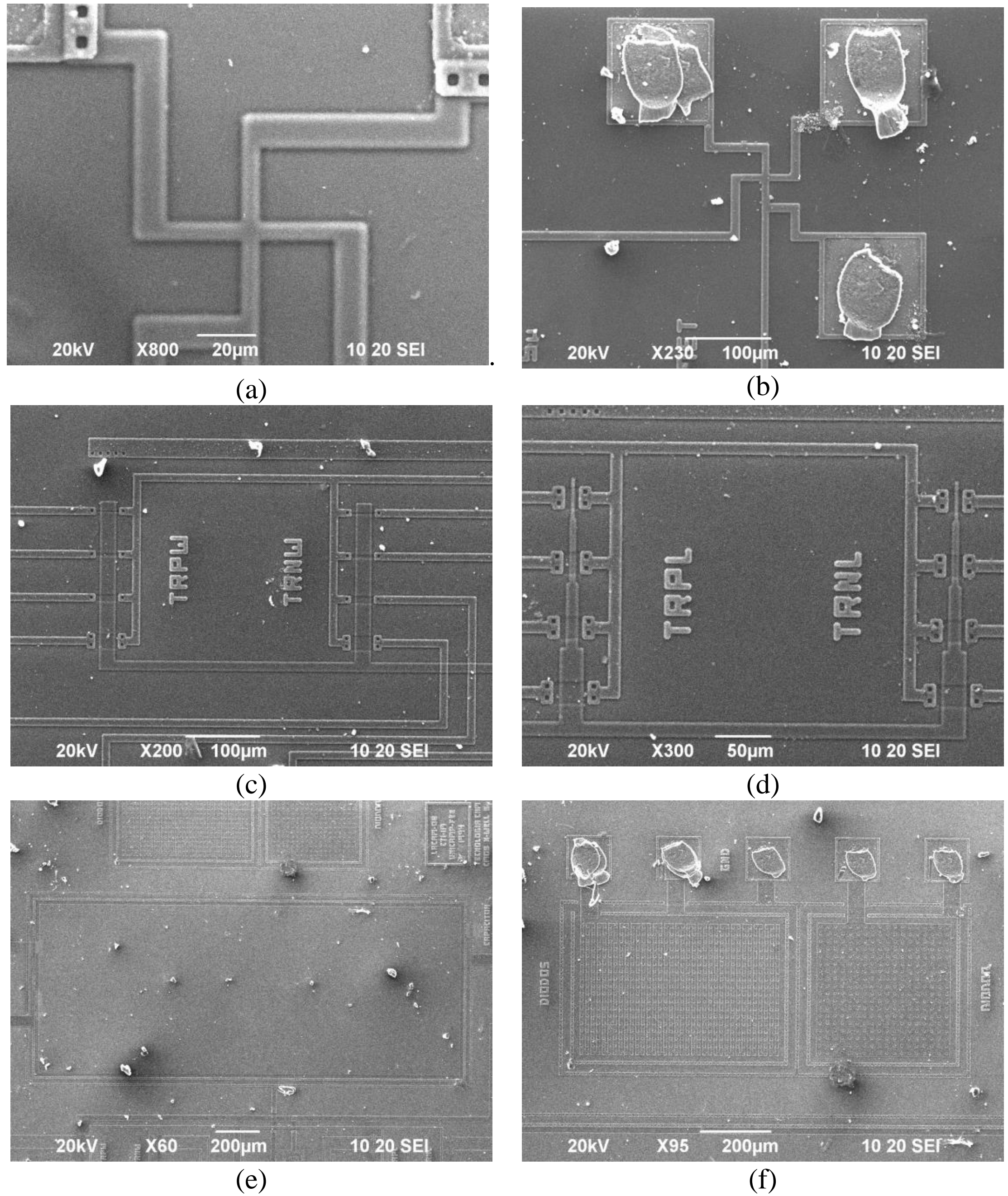


**Fig. 5.**2: Images obtained by SEM on the test chip. a) SEM Micrographs of the devices and structures to polarize of the test chip LACAM-02. (a) Van-der Pauw Structure (polysilicon). Greek –Cross. (b) Structure Van-der Pauw (Metal-Aluminum). Greek – Cross. (c) Transistors PMOS & NMOS with Length Fixed and Width Variable. (d) Transistors PMOS & NMOS with Length Variable and Width Fixed. (e) MOS Capacitor. (f) Diodes (Conventional Square and Serpentine).

Although images obtained of the other structures under different biasing conditions (different voltages, currents, modulation frequencies) are the subject of our current research and will be not described here, in this manuscript we will focus our attention in the Greek cross structure represented in part (a) of Fig. 5.2. This type of structures are widely used in the semiconductor industry for the measurement of sheet resistance [62-65].

## 5.3. Imaging on Polysilicon Tracks.

In the first case of the results obtained in Chapters 3 and 4, the sample excitation is provided by an intensity modulated laser beam, which heats the sample through light absorption. The surface temperature of the sample is probed by a second non-modulated laser, whose intensity changes induced by variations in sample optical reflectance provoked by the periodical heating are detected by a photodiode coupled to a lock-in amplifier. Modulation frequencies are typically in the range of kHz to MHz to bring the characteristic thermal diffusion length to the micrometer scale.

On the other hand, in the case of operating devices, the excitation is generally done by modulated current/voltage applied to the circuit. The non-modulated probe laser beam scans the sample surface to store its thermal image. Resistive tracks, [24,66] MOSFET's, [12,48,49] solar cells, [68] and diode-lasers [18,69-72] were widely investigated. Joule heating is often the dominant mechanism in resistive tracks; [15] electro-reflectance and Seebeck/Peltier contributions were also reported in the devices. [48, 66].

### *5.3.1 Experimental details.*

The resistive tracks are biased with a voltage of the form $V(t) = (V_0/2)[1 + \cos(\omega t)]$, with $\omega = 2\pi f$ and $V_0$ up to 5.0 V. The thermoacoustic signal is acquired by a pyroelectric/piezoelectric sensor, which is the active component of a commercial buzzer (BGD, Steren) connected to a lock-in amplifier. The ensemble sample-PZT (see Fig. 5.3(a)) is placed on a motion stage with minimum step size of 0.1 µm.

The conventional thermal reflectance microscopy is achieved by using an intensity modulated $Ar^+$ laser line as excitation (488 nm, 1.0 µm in diameter, typically few mW at the sample), and a non-modulated He-Ne laser as probe (632.8 nm, 1.2 µm in diameter, typically tens of µW at the sample), both superimposed and focused on the sample surface by an optical microscope. The reflected He-Ne beam is detected by an Si photodiode connected to a lock-in amplifier. Modulation frequencies used both in the voltage and in the excitation $Ar^+$ laser range between f = 25 Hz and 100 kHz. The lock-in selects the 1st or the 2nd harmonic of the signals. The optical image of the sample consisting of polycrystalline silicon resistive tracks (6 µm and 12 µm wide, 0.42 µm thick) on monocrystalline Si substrate fabricated on a test chip is shown in Fig. 5.3(c). In this figure one can also see the metallic contact pads (numbers 1–4) and a metallic track (20 µm wide, 0.60 µm thick, signalized by the arrow) connecting pad number 3 to the polycrystalline silicon track. The resistive tracks are isolated from the substrate by a 0.5 µm thick $SiO_2$ layer. Figure 5.3(b) shown the biasing scheme, and Figure 5.3 (d) shows an electric diagram of the equivalent circuit.

### *5.3.2 Results and Discussion.*

Figure 5.4 shows the photothermal maps obtained by using the $Ar^+$ laser line as excitation (conventional excitation, Chapter 3 and 4), modulated at f = 50 Hz. The scanned area is 200 µm x 200 µm and covers the central part of the trail that includes polycrystalline silicon tracks, as shown in Fig. 5.4 (a).

It has to be observed that the signal detected by the PZT is transmitted across the sample thickness (~300 μm Si substrate followed by ~1 mm backing chip capsule), once the heat generation takes place mostly at the front surface of the chip. The thermal diffusion length in Si (thermal diffusivity a $\propto_{Si} = 0.88$ cm$^2$/s) [17] is $\mu = \left(\frac{\alpha}{\pi f}\right)^2 = 750$ μm at f =50 Hz. It means that a negligible amount of modulated heat reaches the PZT sensor in this case, thus excluding the pyroelectric contribution to the signal.

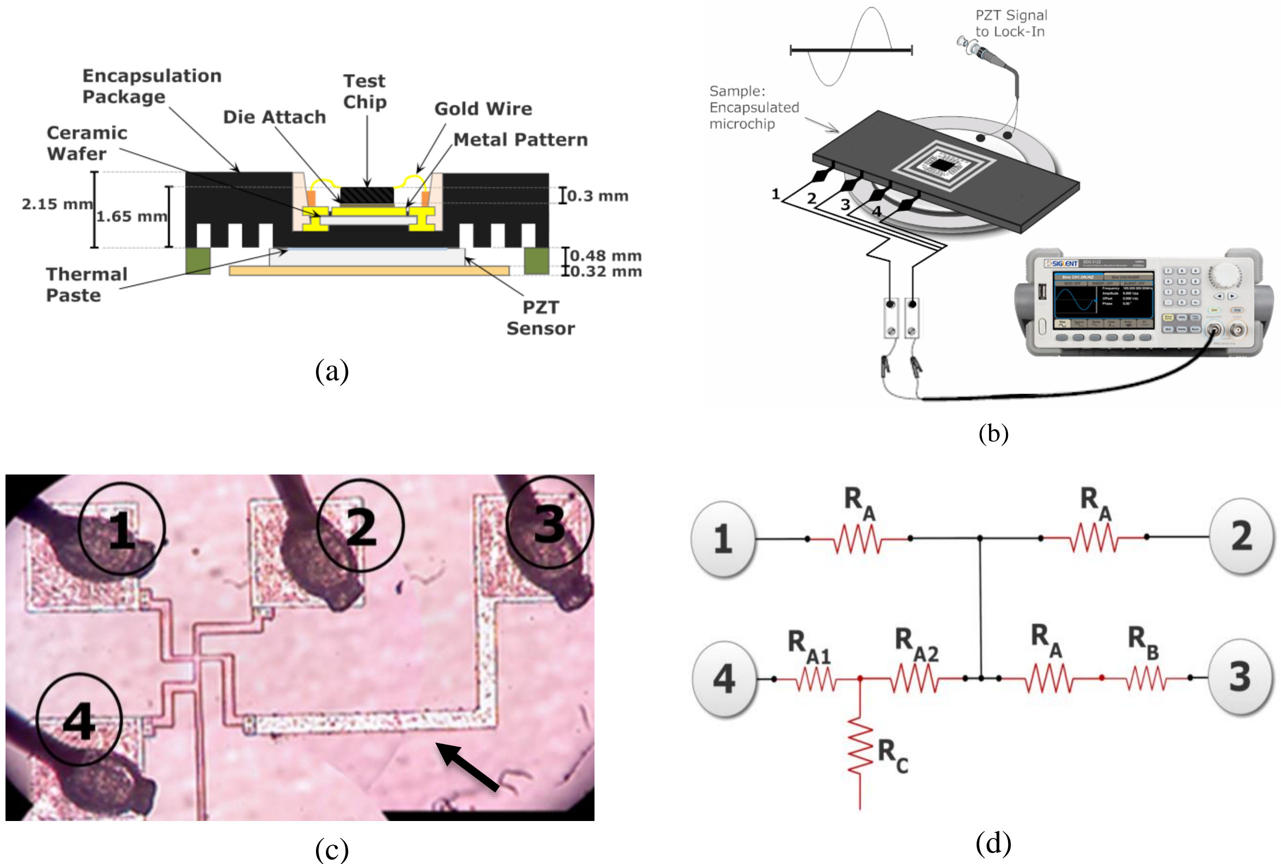


**Fig. 5.3:** Detailed images of Polysilicon Tracks. (a) Cross-sectional scheme of the sample and PZT sensor. (b) Biasing scheme. (c) Optical image of the sample showing the interconnects on an Si substrate and the polycrystalline silicon resistive tracks are 6 μm and 12 μm wide, and 0.42 μm thick. The metallic track is 20 μm wide and 0.60 μm thick. The resistive tracks are isolated from the substrate by a 0.5 μm thick $SiO_2$ layer. (d) Electric diagram of the circuit: $R_A=R_{A1}+R_{A2}=0.32$kΩ, $R_B= 0.07$kΩ, $R_C=1.86$kΩ. The bottom pad (not visible) of the central line with resistance $R_C$ is open (not connected).

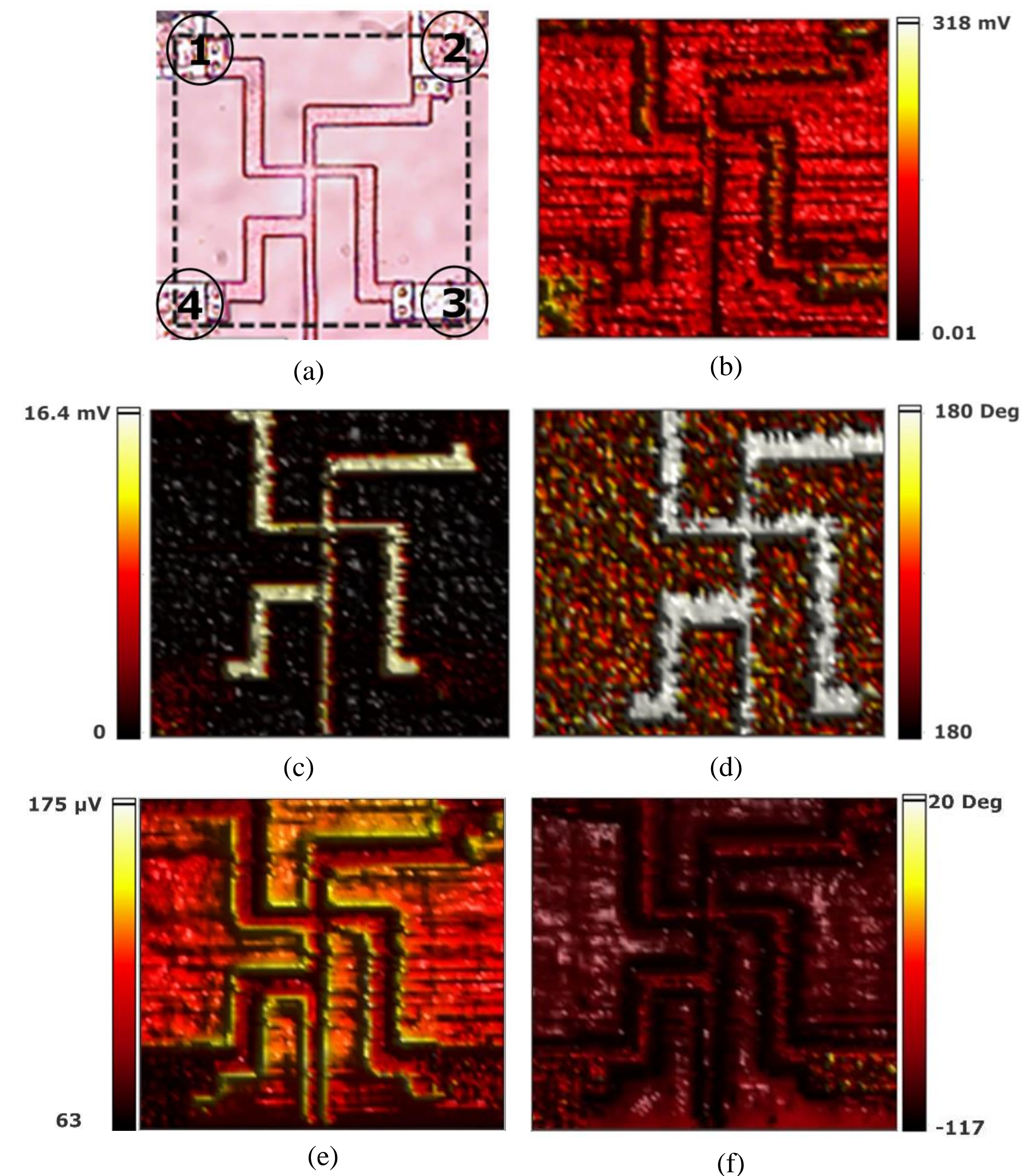


**Fig. 5.4:** PRM and PAM images of Polysilicon Tracks. (a) Optical image of Greek Cross (b) PRM $S_{DC}$ map. (c) PRM amplitude map. (d) PRM phase map; (e) PAM amplitude map and (f) PAM phase map. Scanned area: 200 µm x 200 µm, covering the crossing tracks region of optical image (a). Modulated laser beam (Ar$^+$ laser as excitation, f = 50 Hz). The dotted line marks the scanned area.

The significant contribution comes from the piezoelectric effect produced by centimeter long wavelength acoustic waves that are generated by the laser absorption and subsequent heat production at the top surface of the sample. Here, the contrast displaying the tracks geometry (also observed in the figure 5.4 (d) phase map) expresses the optical absorption differences between the structures formed by polycrystalline silicon-$SiO_2$-Si substrate and by $SiO_2$-Si substrate. However, there are additional effects involved in the contrast definition: (i) the mismatch between the thermal properties of polycrystalline silicon and $SiO_2$ partially confines the heat produced inside the track, while outside heat propagates downward the substrate in an almost spherical way; (ii) acoustic waves produced in the tracks are subjected to reflections at the two interfaces of the silica layer. Actually, when the excitation laser strikes the track, the production of acoustic waves is hardly influenced by the mechanical bond of the whole structure, as well as by the local distinction between its mechanical properties.

In Figure 5.5 presents results on the resistive polycrystalline silicon track biased with a modulated voltage at f = 25 kHz and with $V_0$ = 4.0 V. The scanned area (162 µm x 173 µm) covers the central part of the trail, shown in Fig. 5.5 (a). Voltage bias was applied in pads number 2, 3, and 4, while pad number 1 was kept grounded (see Fig.5.3 (b)). Figures 5.5 (c) and 5.5 (e) display the signal amplitude map and phase map registered at the 2nd harmonic (2f) for PZT and the thermoreflectance detection, respectively.

In order to obtain the PZT image, a 488 nm non-modulated laser beam was used to scan the sample surface. As stated before, the addition of the non-modulated laser creates a supplementary modulated PZT signal component that discriminates the lateral regions of the sample. The image of Fig. 5.5 (e) undoubtedly discloses the resistive tracks structure.

The four branches carrying electric current (connected to pads number 1, 2, 3, and 4) are revealed both in amplitude (higher values on the track and nearby) and in phase (see 5.5 (f)). Moreover, the bottom part of the central vertical line, which does not carry any electric current, is exhibited in the same way (with smaller amplitude).

On the other hand, the metallic pads and the metallic track connected to pad number 3 do not evidence significant contrast. Figure 5.5 (c) must be used as a comparative reference to the PZT map, since the thermoreflectance signal is well established in operating microelectronic devices. It generally reveals the Joule heat dissipation feature of the circuit, being therefore, closely related to the electric current density distribution.

The volumetric heat power density released by Joule effect in the track is given by

$$(\text{power/volume}) = (J^2/\sigma) = \sigma E^2 \tag{5.1}$$

with $\sigma$ being the electric conductivity, and $J$ and $E$ the magnitude of the electric current density and of the electric field, respectively. Therefore, the amount of heat released per unit time and per unit volume is proportional to the square of the applied voltage, $V^2$, and

$$V^2 = (V_0/2)^2\{1+\cos(\omega t)\}^2 = V^2\{(3/8)+(1/2)\cos(\omega t)+(1/8)\cos(2\omega t)\} \tag{5.2}$$

As one can see from Eq. (5.2), the Joule effect presents both the 1st and the 2nd harmonic. Indeed, the 2nd harmonic signal amplitude of the thermoreflectance, with the probe laser on the top of the biased track, follows clearly a $V_0^2$ curve (measurements not shown). Moreover, the local volumetric density of heat dissipation is proportional to the square of the magnitude of the current density (see Eq. (5.1)). This explains the maximum signal amplitude at the left side of the internal cross in Fig. 5.5 (c), which is the narrowest one (6 µm wide) and carries the total electric current supplied by the function generator. Accordingly, smaller signal amplitude is observed at the portion of the track connected to pad number 1, since it is wider than the central part. The signal amplitude is strongly reduced in the other three branches of the internal cross because the electric current is split into the pathways. It is even smaller in the wider parts of the track connected to pads number 2, 3, and 4.

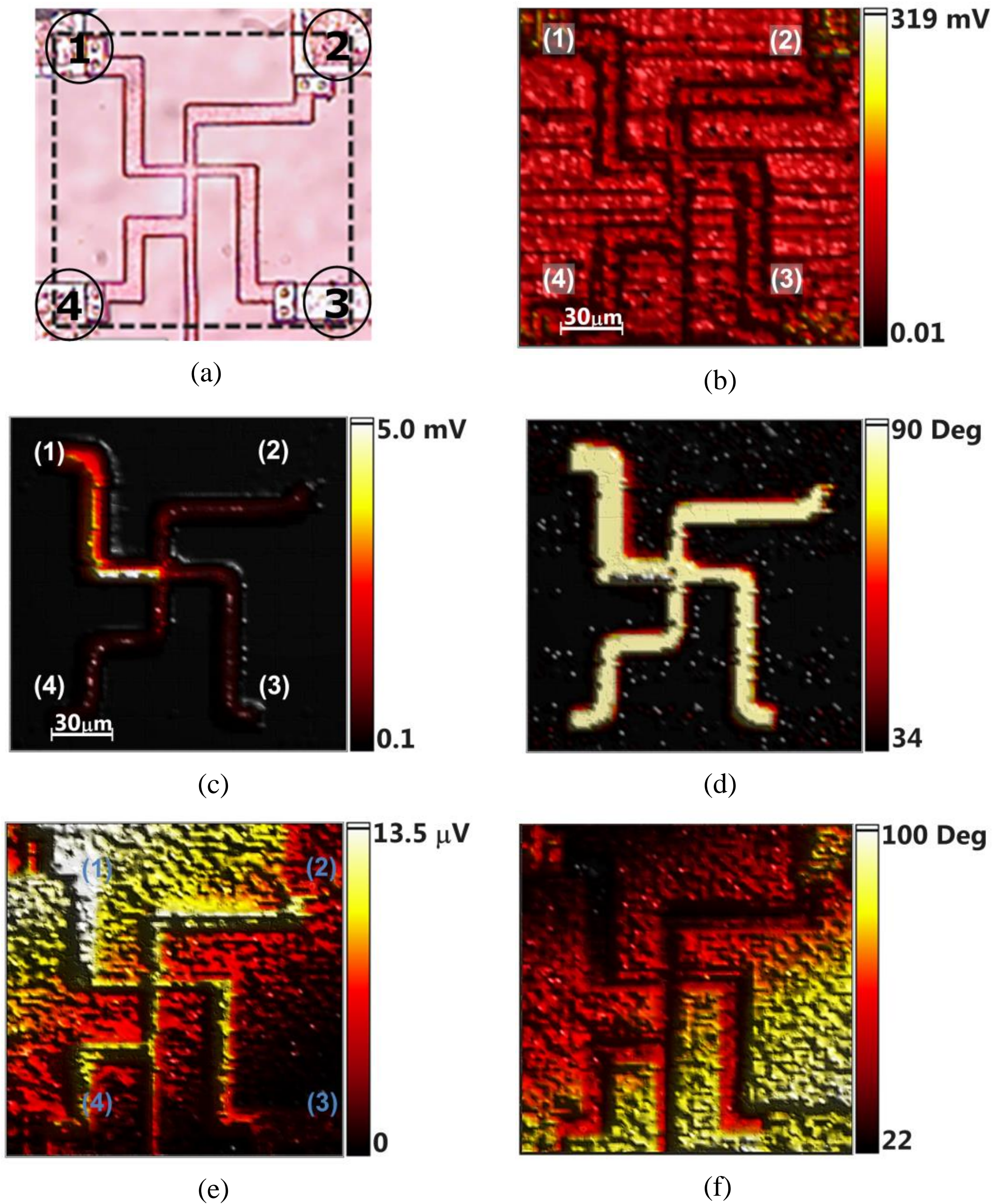


**Fig. 5.5:** Thermoreflectance and thermoacoustic images of Polysilicon Tracks. (a) Optical image of Greek Cross. (b) Thermoreflectance $S_{DC}$ Image. (c) Thermoreflectance signal amplitude map under modulated voltage excitation. (d) Thermoreflectance phase map. (e) Thermoacoustic PZT signal amplitude and (f) Thermoacoustic phase maps PZT.

All images were obtained in the $2^{nd}$ harmonic. Scanned area: 162 μm x 173 μm, covering the crossing tracks region of optical image (a). The Modulated voltage ($V_0$ = 4.0 V, f = 25 kHz) was applied in 2,3,4 pins, keeping pin 1 grounded (see Fig. 1.(b). Non-modulated laser beam: 488 nm, 400 mW. The dotted line marks the scanned area.

Finally, it is easy to observe that the signal amplitude is quite small at the metallic track (signalized by the arrow in Fig. 5.3 (c)), and at the pads themselves. This is explained taking into account the larger size of these structures and the higher thermal and electric conductivity/diffusivity of the metal compared with the polycrystalline silicon. Besides the smaller heat dissipation, the larger size of the tracks facilitates the heat spreading out from the source, thus reducing the local temperature variation.

Mismatch in the temperature coefficient of the reflectance, $\left(\frac{\partial R}{\partial T}\right)$, and optothermal interference phenomena [24, 68] are also involved in the response contrast between poly-crystalline silicon, metal, and Si substrate regions. Indeed, the thermal diffusion length at 25 kHz is 34 μm in silicon and about 3 μm in the SiO2 layer. [72] It means that the heat generated inside the track must spread out to Si substrate through the SiO2 layer, although a significant heat confinement must occur due to thermal properties mismatch between polycrystalline silicon and silica. However, despite the existence of temperature modulation outside the track, the distinct thermo-optical response of the track itself makes the contrast observed in Fig. 5.5 (c), as well as in other reported thermoreflectance measurements on biased tracks (see Ref. 68, for instance), exceptionally sharp.

Going back to the analysis of the PZT signal of Fig. 5.5 (e), it is worth to say that, although the image reveals the tracks feature, the signal amplitude distribution does not match that of Fig. 5.5 (c), i.e., the distribution of electric cur-rent supplied by the function generator. Actually, the bottom part of the central vertical line, represented by $R_C$ in Fig. 5.3, is clearly visible in Fig. 5.5 (e) and definitely does not carry any steady-state electric current.

Even then, the PZT signal is still present both in the 1st and in the 2nd harmonics (the latter depicted in Fig. 5.5 (e)). Furthermore, it scales as the second power of the voltage magnitude, as it can be seen from Fig. 5.6, which shows the PZT 2nd harmonic signal amplitude as a function of the square of the applied voltage $V_0$ at f = 25 kHz. In this figure, the data points represented by squares were obtained without the use of the laser beam (laser off).

This contribution to the PZT signal comes from Joule effect produced in the whole circuit directly by the applied voltage, and constitutes the main part of the back-ground signal of Fig. 5.5 (e). The Joule dissipation at the resistive track at the top of the chip is detected by the PZT, which is located underneath the chip capsule. The thermal diffusion length of Si at 25 kHz is 34 μm, which strongly attenuates the thermal wave transmitted through the substrate and the backing of the chip capsule, until reaching the sensor. Again, the conclusion is that acoustic waves are the dominant mechanism to carry the information from the heat source to the PZT detector, the same as observed in Fig. 5.4.

The triangles in Fig. 5.6 represent measurements made using the non-modulated (laser on), focused out of the tracks (on the substrate), in the central part of the circuit. Indeed, the measured signal at this condition is not dependent on the laser intensity. The dashed line in Fig. 5.6 is the linear best fit to these data (squares and triangles taken altogether), thus indicating their dependence with $V_0^2$.

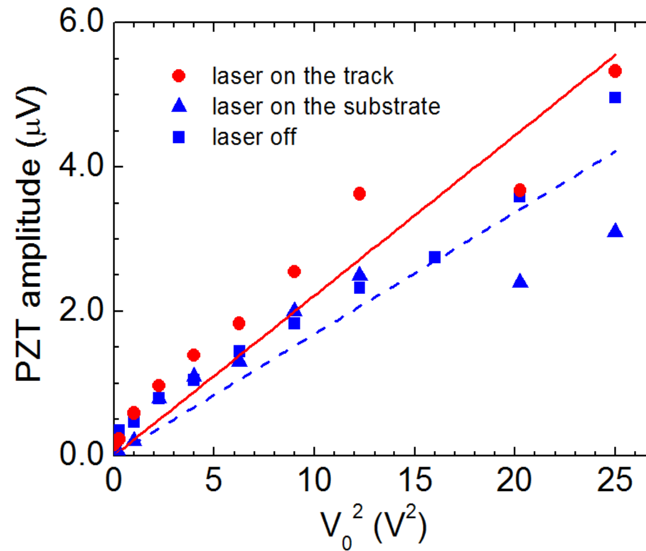


**Fig. 5.6:** PZT 2nd harmonic signal amplitude as a function of the square of the modulated applied voltage $V_0$. Symbols represent measured values. Solid line is the linear best fit to the "laser on the track" data (circles). Dashed line represents the linear best fit to the other measured data altogether (triangles and squares).

The incremental signal that appears when the non-modulated laser strikes the sample becomes particularly significant nearby the resistive tracks. The circles in Fig. 5.6 represent the PZT 2nd harmonic signal amplitude as a function of the square of the applied voltage $V_0$, with the laser hitting the center of the track (under current flow). The solid line is the linear best fit to these data, indicating that the signal still has the quadratic dependence on the applied voltage (Joule effect). Using the fitted curves, it can be seen that the incremental signal is of the order of 30%. This additional contribution to the PZT signal exhibits the tracks conducting electric current, but also those parts without current flow. The contrast comes from the laser absorption in the track and in the close proximity to it. The absorbed light, both by the polycrystalline silicon track and by the silicon substrate in the vicinity of the track, gives rise to the production of local non-modulated heat and electron-hole pairs.

The local modulated electric field along the track, which is responsible for the current flow at first, acts on these photo-injected electrons and holes, accelerating them and producing an additional carrier drift, which is in turn, modulated at the voltage frequency. This longitudinal modulated drift of photo-injected carriers would explain the supplementary signal all the way of the current flow.

The hypothesis of photo-injected carrier modulation is supported by the fact that, on the metallic parts (track and contact pads), the additional contribution is absent. In the case of the branches that do not carry electric current, such as the bottom part of the central vertical line in Fig. 5.5 (e), there is no longitudinal component of the electric field (no longitudinal voltage gradient). However, once a uniform voltage is applied in a certain region of the resistive track, there appears a voltage gradient in the substrate, i.e., an electric field with components parallel and perpendicular to the resistive line, which in turn can modulate the photo-injected carriers at the very close vicinity of the track. In the case of the bottom part of the vertical line of Fig. 5.5 (e), the applied voltage oscillates at the frequency f with intermediate amplitude, since it is connected to the central part of the resistive loop.

The signal level that would come from this potential modulation is also intermediate, as observed from Fig. 5.5 (e). Finally, the background signal in Fig. 5.5 (e), i.e., the signal recorded when the non-modulated laser impinges the Si substrate, far from the conducting tracks, also presents a specific aspect, i.e., it increases towards pad number 1 (the grounded pad). This fact is consistent with the expected distribution of the modulated electric field lines in the Si substrate under the applied bias: the lines originate in the tracks, which are at an elevated potential, and converge to the pad number 1 that is grounded, crossing the semiconductor substrate.

Therefore, the concentration of lines is higher near the pad number 1, as it is the measured signal amplitude. It has to be mentioned that similar behavior was observed when acquiring the PZT signal amplitude map under distinct polarizations, namely, when connecting $V_0$ separately only to pad number 2 (or 3, or 4), or to pairs of pads as 2–3, 2–4, and 3–4, with pad number 1 grounded. In these cases, the overall signal intensity changes, as expected, and the background signal distribution is roughly maintained.

As a final comment, focusing and defocusing of the laser spot when scanning the sample surface is completely excluded considering the measurements of Figs. 5.4 and 5.5 (c) Besides the Joule effect caused by the photo-injected carrier drift (along and perpendicular to the tracks), other possible mechanisms for the PZT signal associated with the non-modulated laser absorption are the carrier recombination, particularly at the materials interfaces, and the generation of acoustic waves by the electric field strength associated to the photo-injected carriers.

Both mechanisms could be present, at the frequency f, in the regions where there is no net current flow in the track. On the other hand, artifacts such as the modulation of the laser absorption produced by the lateral displacement of the track edge (thermal expansion) are far below the noise level. Typical values of such displacement would range between $10^{-6}$ and $10^{-3}$ the size of the beam's spot. This would introduce a signal contribution of the order of $10^{-6}$ – $10^{-3}$ the thermoacoustic signal amplitude of Fig. 5.3, i.e., a signal ranging in the pV-nV scale.

The same applies to the normal (vertical) displacement of the track (change in its thickness). References 18, 24, and 66 report the detection of thermal displacement of sample features (diode laser length, coating layer thickness), using a reflected probe laser beam. Length changes of angstroms 18 and thickness variations of nanometers or less [24, 66] were observed.

However, the extremely high sensitivity in those cases is possible only because the probe beam intensity is modulated by knife edge and interference effects. Finally, one has to notice that the bottom of the central vertical line (characterized by $R_C$ in Fig. 5.3 (c)) does not carry any current, being free of thermal expansion effects. Nonetheless, the thermoacoustic signal is clearly displaying the track feature. The key of the proposed technique is the carrier photo-injection by the non-modulated laser beam. These carriers are, in turn, driven by the applied modulated electric field, thus resulting in heat and acoustic wave production at the located point of the laser absorption. This composed excitation method associated with the acoustic detection proved to be sensitive to the voltage distribution, becoming a complementary technique to the well-established current flow map achieved through thermoreflectance measurements.

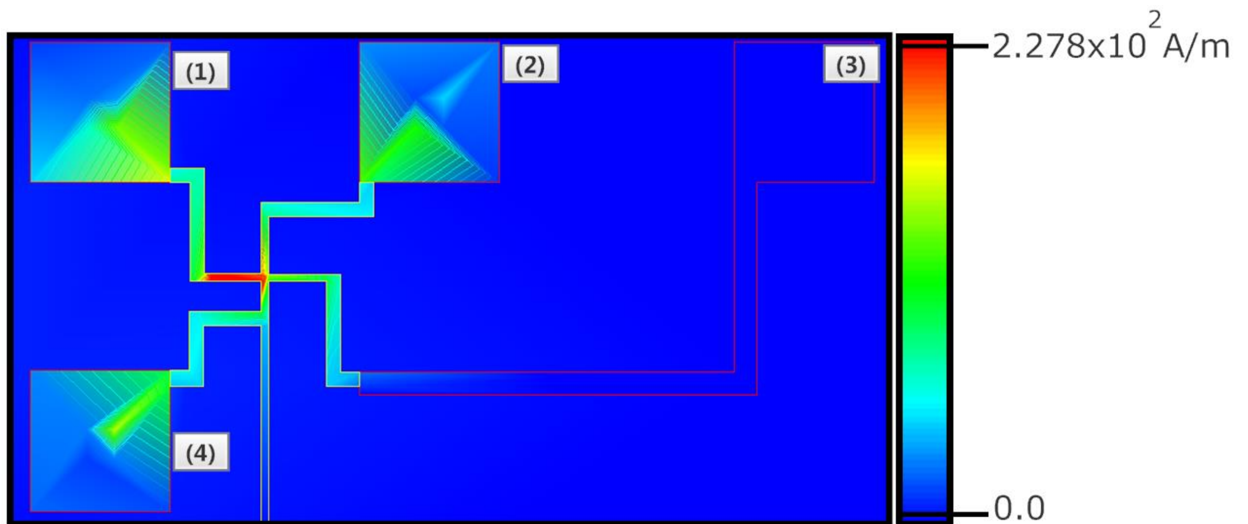


**Fig. 5.7:** Finite elements simulation using Advanced Design Software (ADS)

Figure 5.7 shows the finite elements simulation of the electrical linear current density along the conducting tracks of Fig. 5.3(c) using Advanced Design Software. The current flowing through the vertical line observed in Figs. 5.5(c) and 5.5 (d) is clearly shown.

# Conclusion.

In conclusion, a combined thermoreflectance and thermoacoustic set-up was presented and applied to the imaging of passive and active electronic devices. Two distinct excitation methods were investigated: the conventional modulated laser beam absorption and voltage/current modulation across the circuit. In the first case (modulated laser excitation), the distinct materials structure is revealed through both detection schemes. It is worth to emphasize the excellent sensitivity of the thermoacoustic detection, since the sensor is placed underneath the sample, what makes the excitation point and the sensor distanced by the whole substrate thickness and the chip capsule backing.

The second excitation method (voltage/current modulation) exhibit the current flow through the thermoreflectance detection. The acquisition of a given point of the image is made by placing the probe beam at the desired position on the sample surface. This procedure pinpoints the signal source and allows the image construction. On the other hand, the thermoacoustic detection averages the whole signal coming from the entire sample. Furthermore, the method of excitation heats the whole circuit as well, and no imaging results from this type of measurement. However, the addition of a focused non-modulated laser beam scanning the sample astonishingly showed to be useful in revealing the circuit track structure and the current and voltage distributions.

In resume:

1. A combined modulated photoreflectance and photoacoustic microscopy experimental set-up was build.
2. The microscope was applied for imaging of passive microelectronic devices.
3. The microscope was used for imaging of biased microelectronic devices with thermal wave excitation done by modulated current/voltage applied to the circuits.
4. A combined modulated photoreflectance and photoacoustic microscopy experimental set-up is a useful tool for the characterization of microelectronic devices in operation.

# REFERENCES


**[01]** A. Rosencwaig, *Photoacoustics and photoacoustic spectroscopy*. Wiley, 1980.

**[02]** G. Busse, “Optoacoustic phase angle measurement for probing a metal,” *Applied Physics Letters*, vol. 35, no. 10, pp. 759–760, 1979.

**[03]** A. Rosencwaig and A. Gersho, “Theory of the photoacoustic effect with solids,” *Journal of Applied Physics*, vol. 47, no. 1, pp. 64–69, 1976.

**[04]** P. K. Kuo and L. D. Favro, “A simplified approach to computations of photoacoustic signals in gas-filled cells,” *Applied Physics Letters*, vol. 40, no. 12, pp. 1012–1014, 1982.

**[05]** K. R. Grice, L. J. Inglehart, L. D. Favro, P. K. Kuo, and R. L. Thomas, “Thermal wave imaging of closed cracks in opaque solids,” *Journal of applied physics*, vol. 54, no. 11, pp. 6245–6255, 1983.

**[06]** A. C. Boccara, D. Fournier, and J. Badoz, “Thermo-optical spectroscopy: Detection by the’’mirage effect’’,” *Applied Physics Letters*, vol. 36, no. 2, pp. 130–132, 1980.

**[07]** L. C. Aamodt and J. C. Murphy, “Photothermal measurements using a localized excitation source,” *Journal of Applied Physics*, vol. 52, no. 8, pp. 4903–4914, 1981.

**[08]** F. A. McDonald, G. C. Wetsel Jr, and G. E. Jamieson, “Photothermal beam-deflection imaging of vertical interfaces in solids,” *Canadian Journal of Physics*, vol. 64, no. 9, pp. 1265–1268, 1986.

**[09]** J. Guitonny, Z. Bozoki, A. M. Mansanares, M. Le Liboux, D. Fournier, and A. C. Boccara, “Contrast enhancement in crack detection by stimulated differential infrared radiometry: modelisation and experiments,” *Optics communications*, vol. 104, no. 1–3, pp. 61–64, 1993.

**[10]** G. Busse, “Optoacoustic and photothermal material inspection techniques,” *Applied optics*, vol. 21, no. 1, pp. 107–110, 1982.

**[11]** J. Opsal, A. Rosencwaig, and D. L. Willenborg, “Thermal-wave detection and thin-film thickness measurements with laser beam deflection,” *Applied Optics*, vol. 22, no. 20, pp. 3169–3176, 1983.

**[12]** A. Mandelis, A. Williams, and E. K. Siu, “Photothermal wave imaging of metal-oxide-semiconductor field-effect transistor structures,” *Journal of applied physics*, vol. 63, no. 1, pp. 92–98, 1988.

**[13]** A. Rosencwaig, J. Opsal, W. L. Smith, and D. L. Willenborg, “Detection of thermal waves through optical reflectance,” *Applied Physics Letters*, vol. 46, no. 11, pp. 1013–1015, 1985.

**[14]** J. Opsal and A. Rosencwaig, “Thermal and plasma wave depth profiling in silicon,” *Applied Physics Letters*, vol. 47, no. 5, pp. 498–500, 1985.

**[15]** J. Opsal, M. W. Taylor, W. L. Smith, and A. Rosencwaig, “Temporal behavior of modulated optical reflectance in silicon,” *Journal of applied physics*, vol. 61, no. 1, pp. 240–248, 1987.

**[16]** L. J. Inglehart, A. Broniatowski, D. Fournier, A. C. Boccara, and F. Lepoutre, “Photothermal imaging of copper-decorated grain boundary in silicon,” *Applied physics letters*, vol. 56, no. 18, pp. 1749–1751, 1990.

**[17]** A. M. Mansanares, T. Velinov, Z. Bozoki, D. Fournier, and A. C. Boccara, “Photothermal microscopy: Thermal contrast at grain interface in sintered metallic materials,” *Journal of applied physics*, vol. 75, no. 7, pp. 3344–3350, 1994.

**[18]** A. M. Mansanares, J. P. Roger, D. Fournier, and A. C. Boccara, “Temperature field determination of InGaAsP/InP lasers by photothermal microscopy: Evidence for weak nonradiative processes at the facets,” *Applied physics letters*, vol. 64, no. 1, pp. 4–6, 1994.

[19] J. B. Rojas-Trigos, E. Marin, A. M. Mansanares, E. Cedeno, G. Juarez-Gracia, and A. Calderon, "Theoretical description of the photopyroelectric technique in the slanted detector configuration for thermal diffusivity measurements in fluids," *Thermochimica Acta*, vol. 582, pp. 101–105, 2014.

[20] W. Jackson and N. M. Amer, "Piezoelectric photoacoustic detection: theory and experiment," *Journal of Applied Physics*, vol. 51, no. 6, pp. 3343–3353, 1980.

[21] E. Marín, E. Hernández-Rosales, A. M. Mansanares, R. Ivanov, J. B. Rojas-Trigos, and A. Calderón, "A method for thermal diffusivity measurement in fluids," *Review of Scientific Instruments*, vol. 84, no. 10, p. 104903, 2013.

[22] D. P. Almond and P. Patel, *Photothermal science and techniques*, vol. 10. Springer Science & Business Media, 1996.

[23] A. Mandelis, A. Williams, and E. K. Siu, "Photothermal wave imaging of metal-oxide-semiconductor field-effect transistor structures," *Journal of applied physics*, vol. 63, no. 1, pp. 92–98, 1988.

[24] L. R. De Freitas, E. C. Da Silva, A. M. Mansanares, G. Tessier, and D. Fournier, "Sensitivity enhancement in thermoreflectance microscopy of semiconductor devices using suitable probe wavelengths," *Journal of applied physics*, vol. 98, no. 6, p. 063508, 2005.

[25] S. P. Albright, B. Ackerman, and J. F. Jordan, "Efficient CdTe/CdS solar cells and modules by spray processing," *IEEE transactions on Electron Devices*, vol. 37, no. 2, pp. 434–437, 1990.

[26] K. Martínez *et al.*, "Thermal diffusivity measurements in solids by photothermal infrared radiometry: Influence of convection–radiation heat losses," *International Journal of Thermal Sciences*, vol. 98, pp. 202–207, 2015.

[27] J. A. Rich, L. E. Prescott, and J. D. Cobine, "Anode Phenomena in Metal-Vapor Arcs at High Currents," *Journal of Applied Physics*, vol. 42, no. 2, pp. 587–601, 1971.

[28] R. A. Hartunian and R. L. Varwig, "On Thin-Film Heat-Transfer Measurements in Shock Tubes and Shock Tunnels," *The Physics of Fluids*, vol. 5, no. 2, pp. 169–174, 1962.

[29] R. L. Thomas, L. D. Favro, and P. K. Kuo, "Thermal-wave imaging for nondestructive evaluation," *Canadian Journal of Physics*, vol. 64, no. 9, pp. 1234–1237, 1986.

[30] A. P. Neto, H. Vargas, N. F. Leite, and L. C. M. Miranda, "Photoacoustic characterization of semiconductors: Transport properties and thermal diffusivity in GaAs and Si," *Physical Review B*, vol. 41, no. 14, p. 9971, 1990.

[31] J. R. D. Pereira, A. M. Mansanares, E. C. Da Silva, A. J. Palangana, M. L. Baesso, and F. Scudieri, "Thermal diffusivity measurements in lyotropic ferronematics: Mode mismatched thermal lens," in *AIP Conference Proceedings*, 1999, vol. 463, pp. 345–347.

[32] M. Reichling and H. Grönbeck, "Harmonic heat flow in isotropic layered systems and its use for thin film thermal conductivity measurements," *Journal of applied physics*, vol. 75, no. 4, pp. 1914–1922, 1994.

[33] G. Langer, J. Hartmann, and M. Reichling, "Thermal conductivity of thin metallic films measured by photothermal profile analysis," *Review of Scientific Instruments*, vol. 68, no. 3, pp. 1510–1513, 1997.

[34] R. E. Taylor, "Thermal conductivity determinations of thermal barrier coatings," *Materials Science and Engineering: A*, vol. 245, no. 2, pp. 160–167, 1998.

[35] M. F. Soonawala, "Thermal Conductivity of water," *Indian J. Phys*., 18, 71-3, 1944

[36] N. Morioka, A. Yarai, and T. Nakanishi, "Thermal diffusivity measurement of liquid samples by inverse photopyroelectric detection," *Japanese journal of applied physics*, vol. 34, no. 5S, p. 2579, 1995.

[37] J. A. P. Lima *et al.*, "On the use of the thermal wave resonator cavity sensor for monitoring hydrocarbon vapors," *Review of Scientific Instruments*, vol. 71, no. 7, pp. 2928–2932, 2000.

[38] C. A. S. Lima, L. C. M. Miranda, and H. Vargas, "Photoacoustics of Two-Layer Systems: Thermal Properties of Liquids and Thermal Wave Interference," *Instrumentation Science and Technology*, vol. 34, no. 1–2, pp. 191–209, 2006.

[39] S. Delenclos, D. Dadarlat, N. Houriez, S. Longuemart, C. Kolinsky, and A. Hadj Sahraoui, "On the accurate determination of thermal diffusivity of liquids by using the photopyroelectric thickness scanning method," *Review of scientific instruments*, vol. 78, no. 2, p. 024902, 2007.

[40] J. A. P. Lima *et al.*, "Measurement of the thermal properties of liquids using a thermal wave interferometer," *Measurement Science and Technology*, vol. 11, no. 10, p. 1522, 2000.

[41] I. A. Esquef, A. P. L. Siqueira, M. G. da Silva, H. Vargas, and L. C. M. Miranda, "Photothermal gas analyzer for simultaneous measurements of thermal diffusivity and thermal effusivity," *Analytical chemistry*, vol. 78, no. 14, pp. 5218–5221, 2006.

[42] A. Rosencwaig, "Photoacoustic spectroscopy of solids," *Optics Communications*, vol. 7, no. 4, pp. 305–308, 1973.

[43] Y. H. Wong, R. L. Thomas, and G. F. Hawkins, "Surface and subsurface structure of solids by laser photoacoustic spectroscopy," *Applied Physics Letters*, vol. 32, no. 9, pp. 538–539, 1978.

[44] A. P. Neto, H. Vargas, N. F. Leite, and L. C. M. Miranda, "Photoacoustic investigation of semiconductors: influence of carrier diffusion and recombination in PbTe and Si," *Physical Review B*, vol. 40, no. 6, p. 3924, 1989.

[45] C. Munakata, N. Honma, and H. Itoh, "A non-destructive method for measuring lifetimes for minority carriers in semiconductor wafers using frequency-dependent ac photovoltages," *Japanese Journal of Applied Physics*, vol. 22, no. 2A, p. L103, 1983.

[46] S. Gupta, R. Kaur, S. Garg, and F. Ahmed, "A general theory of an intensity-modulated beam method for determination of diffusion length, diffusion constant, lifetime, surface recombination velocity and absorption coefficient in a semiconductor material," *Solid-state electronics*, vol. 31, no. 9, pp. 1401–1407, 1988.

[47] A. Mandelis, A. Othonos, C. Christofides, and J. Boussey-Said, "Non-contacting measurements of photocarrier lifetimes in bulk-and polycrystalline thin-film Si photoconductive devices by photothermal radiometry," *Journal of applied physics*, vol. 80, no. 9, pp. 5332–5341, 1996.

[48] J. A. Batista, A. M. Mansanares, E. C. Da Silva, and D. Fournier, "Photothermal and electroreflectance images of biased metal-oxide-semiconductor field-effect transistors: Six different kinds of subsurface microscopy," *Journal of applied physics*, vol. 82, no. 1, pp. 423–426, 1997.

[49] J. A. Batista, A. M. Mansanares, E. C. Da Silva, M. B. C. Pimentel, N. Jannuzzi, and D. Fournier, "Subsurface microscopy of biased metal-oxide-semiconductor field-effect-transistor structures: photothermal and electroreflectance images," *Sensors and Actuators A: Physical*, vol. 71, no. 1–2, pp. 40–45, 1998.

[50] G. Tessier *et al.*, "High resolution thermoreflectance imaging on transistor arrays with defect-induced leakage," in *Journal de Physique IV (Proceedings)*, 2005, vol. 125, pp. 423–425.

[51] E. Welsch, M. Reichling, C. Göbel, D. Schäfer, and E. Matthias, "Modulated thermoreflectance imaging of hidden electric current distributions in thin-film layered structures," *Applied physics letters*, vol. 61, no. 8, pp. 916–918, 1992.

[52] P. Voigt, J. Hartmann, and M. Reichling, "Thermal wave imaging of electrically heated microstructures," *Journal of applied physics*, vol. 80, no. 4, pp. 2013–2018, 1996.

[53] F. A. McDonald, "Photoacoustic effect and the physics of waves," *American Journal of Physics*, vol. 48, no. 1, pp. 41–47, 1980.

[54] R. Ivanov, E. Marin, I. Moreno, and C. Araujo, "Electropyroelectric technique for measurement of the thermal effusivity of liquids," *Journal of Physics D: Applied Physics*, vol. 43, no. 22, p. 225501, 2010.

[55] D. Rémiens, "Pyroelectric Materials and Sensors," *Research Signpost, Kerala, India*, 2007.

[56] C. L. Cesar, H. Vargas, and L. C. M. Miranda, "Photoacoustic microscopy of layered samples: phase-detection technique," *Journal of Physics D: Applied Physics*, vol. 18, no. 4, p. 599, 1985.

[57] R. J. Von Gutfeld and R. L. Melcher, “20-MHz acoustic waves from pulsed thermoelastic expansions of constrained surfaces,” *Applied Physics Letters*, vol. 30, no. 6, pp. 257–259, 1977.

[58] Ernesto Hernandez Rosales. Master's Thesis “Aplicación del método de Angstrom para la caracterización térmica de fluidos”. Co-author’s: Marín Moares Ernesto, Juárez Gracia Antonio Gustavo, Thesis Repository of Instituto Politécnico Nacional. 2013.

[59] E. Hecht, Optics, 2ed. New York: Addison Wesley Publishing Company, 1990. 676p.

[60] Celio Costa Vaz. Doctor's Thesis. Analise Termo-Optica de Sistemas Multicamada de uso Espacial ITA. Campo Montenegro, Sao Jose dos Campos, SP, Brasil 2000

[61] Jerias Alves Batista. Doctor's Thesis. Detecção de defeitos em estruturas semicondutoras através da Microscopia Fototérmica de Reflexão: a interferência optotérmica e o aumento de contraste. Universidade Estadual de Campinas, UNICAMP, Brasil.

[62] S. Enderling *et al.*, “Sheet resistance measurement of non-standard cleanroom materials using suspended Greek cross test structures,” *IEEE Transactions on Semiconductor Manufacturing*, vol. 19, no. 1, pp. 2–9, 2006.

[63] M. G. Buehler and W. R. Thurber, “An experimental study of various cross sheet resistor test structures,” *Journal of The Electrochemical Society*, vol. 125, no. 4, pp. 645–650, 1978.

[64] G. P. Carver, R. L. Mattis, and M. G. Buehler, *Design considerations for the cross-bridge sheet resistor*. 1982.

[65] W. Versnel, “Analysis of the Greek cross, a Van der Pauw structure with finite contacts,” *Solid-State Electronics*, vol. 22, no. 11, pp. 911–914, 1979.

[66] B. C. Forget, S. Grauby, D. Fournier, P. Gleyzes, and C. Boccara, “High resolution AC temperature field imaging,” *Electronics letters*, vol. 33, no. 20, pp. 1688–1689, 1997.

[67] M. Mieszkowski and A. Mandelis, “Photopyroelectric spatially resolved imaging of thermal wave fields,” *JOSA A*, vol. 7, no. 4, pp. 552–557, 1990.

[68] J. A. Batista, A. M. Mansanares, E. C. da Silva, C. C. Vaz, and L. C. M. Miranda, “Contrast enhancement in the detection of defects in transparent layered structures: The use of optothermal interference technique in solar cell investigation,” *Journal of Applied Physics*, vol. 88, no. 9, pp. 5079–5086, 2000.

[69] P. W. Epperlein, “Micro-temperature measurements on semiconductor laser mirrors by reflectance modulation: A newly developed technique for laser characterization,” *Japanese journal of applied physics*, vol. 32, no. 12R, p. 5514, 1993.

[70] A. M. Mansanares, M. L. Baesso, E. C. Da Silva, F. C. G. Gandra, H. Vargas, and L. C. M. Miranda, “Photoacoustic and ESR studies of iron-doped soda-lime glasses: thermal diffusivity,” *Physical Review B*, vol. 40, no. 11, p. 7912, 1989.

[71] L. C. O. Dacal, A. M. Mansanares, and E. C. Da Silva, “Heat source distribution, vertical structure, and coating influences on the temperature of operating 0.98 μm laser diodes: Photothermal reflectance measurements,” *Journal of applied physics*, vol. 84, no. 7, pp. 3491–3499, 1998.

[72] A. M. Mansanares, D. Fournier, and A. C. Boccara, “Temperature measurements of telecommunication lasers on a micrometre scale,” *Electronics Letters*, vol. 29, no. 23, pp. 2045–2047, 1993.

## APPENDIX A LIST OF FIGURES


| | Chapter 1 |
|---|---|
| **Figure 1.1** | A homogeneous solid Semi-infinite uniformly illuminated with a modulated radiation flux at the surface x = 0. |
| **Figure 1.2** | PA signal at a phase $\psi$ expressed as the sum of the signal at $0^{\circ}$ and $90^{\circ}$ phases. |
| | **Chapter 2** |
| **Figure 2.1** | Experimental arrangement of Photoacoustic Microscopy, with piezoelectric detection. |
| **Figure 2.2** | Scheme of the experimental set-up for photothermal reflectance microscopy using an $Ar^{+}$ laser as an excitation. |
| **Figure 2.3** | Scheme of the experimental set-up for photothermal reflectance microscopy in microelectronic devices, using the sample as excitation source. |
| **Figure 2.4** | Experimental arrangement mounted of PAM (thermoreflectance and thermoacoustic). |
| | **Chapter 3** |
| **Figure 3.1** | Architecture of SCC. |
| **Figure 3.2** | A smart card pinout. |
| **Figure 3.3** | Optical images of SCC used. |
| **Figure 3.4** | Images obtained from an SCC using PAM with piezoelectric detection. Laser hits in the front surface of the SCC. |
| **Figure 3.5** | Images obtained from an SCC using PAM with piezoelectric detection.<br>Laser hits in the back surface of the SCC. |
| **Figure 3.6** | Images obtained through of Phase-Resolved method using PAM. |
| | **Chapter 4** |
| **Figure 4.1** | Architecture of a SCA in detail. |
| **Figure 4.2** | Optical image and description of naked SCA. |
| **Figure 4.3** | Images of a naked SCA using PRM and PAM in the grid section. |
| **Figure 4.4** | Images of a naked SCA using PRM and PAM in the metallic contact (cross form). |
| **Figure 4.5** | Optical image of unencapsulated chip used to obtain images by PRM and PAM. |
| **Figure 4.6** | Front surface images of a small region (200 µm x 151 µm) of an un-encapsulated chip-01. showing in the center a characteristic Y-shaped track (surface and subsurface tracks). |
| | **Chapter 5** |
| **Figure 5.1** | Detailed images of the test chip. |
| **Figure 5.2** | Images obtained by SEM on the test chip. |
| **Figure 5.3** | Detailed images of Polysilicon Tracks. |
| **Figure 5.4** | PRM and PAM images of Polysilicon Tracks. |
| **Figure 5.5** | Thermoreflectance and thermoacoustic images of Polysilicon Tracks. |
| **Figure 5.6** | PZT $2^{nd}$ harmonic signal amplitude as a function of the square of the modulated applied voltage. |
| **Figure 5.7** | Shows the finite elements simulation of the electrical linear current density along the conducting tracks. |


## APPENDIX B LIST OF TABLES


| | |
|---|---|
| **Tabla 2.1** | Radius of pump beam and probe beam. |
| **Tabla 5.1** | Physical characteristics of the naked SCA. |